THE INTERACTION OF MODERATELY STRONG SHOCK WAVES WITH THICK PERFORATED WALLS OF LOW POROSITY

by Daniel J. Grant

Goddard Space Flight Center
Greenbelt, Md. 20771

NATIONAL AERONAUTICS AND SPACE ADMINISTRATION • WASHINGTON, D. C. • AUGUST 1972

1. Report No.	2. Government Accession No.	3. Recipient's Catalog No.
NASA TN D-6902		

4. Title and Subtitle

The Interaction of Moderately Strong Shock Waves With Thick Perforated Walls of Low Porosity

5. Report Date: August 1972

6. Performing Organization Code:

7. Author(s): Daniel J. Grant

8. Performing Organization Report No.: G-1069

9. Performing Organization Name and Address

Goddard Space Flight Center
Greenbelt, Maryland 20771

10. Work Unit No.:

11. Contract or Grant No.:

12. Sponsoring Agency Name and Address

National Aeronautics and Space Administration
Washington, D.C. 20546

13. Type of Report and Period Covered: Technical Note

14. Sponsoring Agency Code:

15. Supplementary Notes

16. Abstract

This study is concerned with the theoretical prediction of the flow through thick perforated walls of low porosity resulting from the impingement of a moderately strong (M_I = 2 to 5) traveling shock wave. The model was a flat plate positioned normal to the direction of the flow. Holes bored in the plate parallel to the direction of the flow provided nominal hole length-to-diameter ratios of 10:1 and an axial porosity of 25 percent of the flow-channel cross section.

The flow field behind the reflected shock wave was assumed to behave as a reservoir producing a quasi-steady duct flow through the model. Rayleigh and Fanno duct-flow theoretical computations for each of three possible auxiliary-wave patterns that can be associated with the transmitted shock (to satisfy contact-surface compatibility) were used to provide bounding solutions as an alternative to the more complex influence coefficients method.

Qualitative and quantitative behavior was verified in a 1.5- by 2.0-in. helium shock tube. High-speed schlieren photography, piezoelectric pressure-time histories, and electronic-counter wave-speed measurements were used to assess the extent of correlation with the theoretical flow models. Reduced data indicated the adequacy of the bounding-theory approach to predict wave phenomena and quantitative response.

17. Key Words (Selected by Author(s))	18. Distribution Statement
Traveling Waves Shock Waves Shock Tubes Fluid Dynamics Shock Phenomena	Unclassified—Unlimited

19. Security Classif. (of this report)	20. Security Classif. (of this page)	21. No. of Pages	22. Price*
Unclassified	Unclassified	54	$3.00

*For sale by the National Technical Information Service, Springfield, Virginia 22151.

FOREWORD

The research effort reported herein was authorized and funded by the Chemical Propulsion Division, Office of Advanced Research and Technology, National Aeronautics and Space Administration. The author wishes to express his sincere appreciation for this support.

The report is based on a dissertation submitted to the Faculty of the Graduate School of the University of Maryland in partial fulfillment of the requirements for the degree of Doctor of Philosophy.

CONTENTS

LIST OF SYMBOLS

a	area ratio = $1/\epsilon = A_4/A_E$
A	area
${}_mA_n$	area ratio A_m/A_n
C	speed of sound
C_d	orifice discharge coefficient
${}_jC_i$	sound speed ratio = C_j/C_i
C_p	specific heat at constant pressure
C_v	specific heat at constant volume
d	hole or perforation diameter
f	friction factor
F_f	influence coefficient for friction
F_i	thrust function at region i
F_{T_0}	influence coefficient for T_0 change
g	acceleration of gravity
h_e	effective heat transfer coefficient for convection
J	mechanical equivalent of heat unit
k_f	thermal conductivity for the duct-wall film temperature
L	length of the model in direction of the incident wave
$\bar{M}$	molecular weight; mean Mach number
M_I	Mach number of the incident shock wave
${}_m(M_I)_n$	Mach number measured over the interval m to n
M_T	Mach number of the primary transmitted wave
Nu	Nusselt number = $h_e d/k$
p	absolute pressure

${}_yp_x$	pressure ratio = p_y/p_x
P	hole pitch
Pr	Prandtl number = $\mu C_p/k$
$\dot{q}$	heat flux rate
R	individual gas constant = $\bar{R}/\bar{M}$
$\bar{R}$	universal gas constant
Re	Reynolds number = $\rho ud/\mu$
s	entropy
S_I	incident-wave shock strength = p_2/p_1
S_R	reflected-wave shock strength = p_3/p_1
S_T	transmitted-wave shock strength = p_6/p_1
T	absolute temperature
${}_yT_x$	temperature ratio T_y/T_x
u	particle flow velocity
U	shock-wave velocity
U_C	contact-surface velocity
$\dot{w}$	mass flow rate
x	distance parameter in direction of flow
X	heat transfer parameter, defined by Equation 12
Z	compressibility factor in modified van der Waals gas law
γ	specific heat ratio = C_p/C_v
Δ	distance from duct entry to plane of reattachment of vena contracta; increment
ϵ	porosity of model face=area of holes divided by area of flow channel
μ	dynamic viscosity
ρ	density

Subscripts

$0i$	stagnation conditions at station i
1	conditions in rest region
2	conditions behind incident wave

3 conditions behind reflected incident wave

4 conditions at the plane of base region expansion

5 conditions downstream of the auxiliary transmitted shock wave

6 conditions upstream of the primary transmitted shock wave

B conditions at the base region in the exit plane

E conditions at the duct exit plane

F denotes a Fanno process function

R conditions at the duct entry plane; characteristic of reflected shock wave

Ray denotes a Rayleigh process function

Superscript

* denotes parameter on loci of states in compressible flow processes where the Mach number $= u/C = 1$

THE INTERACTION OF MODERATELY STRONG SHOCK WAVES WITH THICK PERFORATED WALLS OF LOW POROSITY

by

Daniel J. Grant
Goddard Space Flight Center

INTRODUCTION

The present work is concerned with a means of theoretically predicting the interaction of a traveling plane shock wave with a thick perforated wall. The flows produced within the perforations, after the plane wave reflects from the upstream face of the plate, are influenced by the combined effects of heat transfer to the wall and friction with the wall. These effects attenuate the strength of the transmitted wave and, therefore, enable the plate to function as a wave suppressor. These same effects were first considered in the quenching of detonation waves in coal-gas/air mixtures.

Systematic research of the phenomena of flashback (unstable combustion in which the flame front propagates back through a fuel feed device and into the fuel supply system) in combustible gas mixtures has been reported as early as 1815 by Sir Humphry Davy (Reference 1) in his investigation of coal mine gas explosions. His experiments on the quenching of coal-gas/air combustion waves by small-diameter tubes and fine mesh wire gauze resulted in his invention of the miner's safety lamp. He was one of the first to recognize the importance of the ratio L/d and heat transfer in suppressing flashback. Over one century later, Payman and Wheeler (Reference 2) investigated the effects of flame speed, tube conductivity, and mixture ratio on quenching distances by means of similar wave-attenuation experiments. Later work (References 3 to 5) further emphasized heat transfer and throttling aspects of narrow channels intended as flashback arrestors in burners or torch tips.

Flashback-type instabilities can occur in rocket chambers using premixed gaseous propellants. The thermodynamics and fluid dynamics of these devices are further complicated by the chemical reaction occurring behind the detonation waves plus the complex perturbations of the flame velocity resulting from interactions with pressure waves reflected from chamber walls and injector faces (Reference 6).

The simplified theoretical model used in the present work considers the flow through an idealized injector plate (a metering device that introduces and controls the flow of fluid propellants to a reaction chamber) produced by the impingement of a traveling shock wave in a nonreactive gas. Such a model is necessary in order to predict the attenuation factors for pressure and temperature resulting from interaction of the incident wave with the face of the injector plate. Combining the results from this study with combustion kinetics and considering the transient heat balance, a numerical

computational approach may be developed for the design of injectors for pulse-mode reactors using premixed gaseous propellants such that a specified duty cycle can be used without experiencing flashback through the injector to the supply line.

The attenuation of traveling waves by structural elements has been examined by previous researchers using shock-tube facilities. The difficulty of obtaining a rigorous theoretical approach to the problem can be appreciated when the complexities and ambiguities associated with shock impingements on a simple area convergence are considered (Reference 7). As a consequence, most studies have been experimental, emphasizing the facility design and instrumentation techniques and primarily seeking fundamental theory on wave dynamics in selected flow channels.

Other investigators have used simplified analytical approaches with varying degrees of experimental correlation. Glass and Patterson (Reference 8) demonstrated the slowing down of reflected shock waves by screens using a schlieren streak record. Bowman and Niblett (Reference 9) determined wave velocities from schlieren photographs of shock-tube plane waves acting upon a woven wire grid of high porosity for a single shock strength (S = 1.65 in air). Dosanjh (Reference 10) used a hot-wire-triggered chronograph to measure incident-, reflected-, and transmitted-wave speeds. Shadowgraphs of the reflected and transmitted waves were taken for grids having 75 percent porosity ratio. The primary purpose of the work was to study shock-wave interaction with a turbulent-flow field produced by a grid in a shock tube. The shadowgraphs provided definitive evidence of auxiliary transmitted-wave formation resulting from base-region effects accompanying choked flow through the grids.

Barthel (Reference 11) was concerned with the attenuation of blast waves by rigid grids to protect structures. He proposed a simplified mathematical flow model to consider theoretically the type of flows that Dosanjh had studied on an empirical basis because of the complexity of the field discharged from the grid. Barthel's mathematical model was based on the consideration of the overall wave pattern and the local flow pattern in the vicinity of his constrictions.. At some distance from his grid, the flow was assumed to be represented by one-dimensional wave-interaction concepts. Flow through the grid was based on compressible, one-dimensional steady flow. By considering the compatibility conditions of flow fields behind and in front of each plane wave generated as a result of shock impingement with the model, a trial and error method was used to compute the strength of the reflected and transmitted waves. For Barthel's analysis, one-dimensional isentropic flow was assumed to exist in the grid. Since his grids were very thin, the residence times of the grid flows were low and the assumption of adiabatic conditions was not too unreasonable. In the Mach number range 1.0 to 2.2, he obtained correlation between predicted and experimental reflected-wave overpressure ratios for round-hole grids with sharp edges having 40 and 72.3 percent open area; however, on prediction of the transmitted overpressures, the correlation was poor in the Mach number range of 1.6 to 2.2, or where choked conditions existed in the grid. This work of Barthel, Dosanjh, and the others (References 7 to 11) was performed with passage length-to-diameter ratios (L/d) of 1 or less.

Crist (Reference 12), concerned with blast wave attenuation in ventilator systems using rock-bed filters, showed that attenuation ratios became independent of bed length when the length was increased to twice the bed diameter. A lesser dependence on void volume ratio was also demonstrated in limited experiments with simple area convergence of the ventilator shaft, using L/d ratios of 8 and 24 and a fixed length of 4 ft; improved attenuation was evidenced with the smaller openings. This

situation is closely allied to the case of an injector plate with orifice L/d values of about 10:1 and open area ratios of 25 percent or less.

The present study makes use of pertinent experimental techniques and theoretical considerations to formulate a mathematical flow model for moderately high wave speeds and thick walls with low porosity.

THEORETICAL BACKGROUND AND FLOW MODEL

It is assumed that the conditions produced by the reflection of the incident shock wave yield upstream reservoir conditions that will supply the flow through the idealized injector for a period of time sufficiently long to approximate steady-flow conditions. Rudinger (Reference 13) and others have shown that shock tubes produce appreciable periods of steady flow through short-duct elements for low incident-wave Mach numbers. With strong shock waves, the transient periods required for gas transport through the longer injector models and for base-pressure adjustment are still only a small fraction of the total steady period that will exist before the reflected incident wave collides with its upstream contact surface or reflected expansion wave.

The effects of heat transfer to the injector plate and turbulent friction in the injector plate will be considered in the calculations to predict the reflected and transmitted waves and the conditions of state behind them. In the range of incident-wave speeds selected, the pressure ratios across the model faces will be such that choked flow will exist in every case. A quasi-steady one-dimensional approach will be used to define regions upstream from the perforated wall and to define flow through the constricted passages and in the downstream regions. Base-region flows will also be evaluated in terms of steady-state conditions and will be the final relatively steady conditions that will exist after the brief interval of time required for secondary flows in the base region to stabilize. The flow in the base region can either lower or raise the base-region pressure with respect to initial conditions depending upon incident-wave strength; this transient phenomenon will be referred to as base-region pumping. This study is confined to incident-wave Mach numbers of 2 to 5, open area or porosity ratios of 25 percent, and L/d of approximately 10. Dry nitrogen gas will be used as the fluid medium.

As has been observed with screens and thin gridlike structures (References 9 to 11), the complex wavelet pattern, which is established immediately after wave impingement, coalesces at some distance from the grid to form a one-dimensional system. With thick perforated walls of high solidity and moderately high incident-wave Mach numbers, similar wave patterns are expected with increased turbulence in the contact flows and adjustments in base flow as a consequence of the higher stagnation pressures and greater base areas.

Therefore, the basis for examination of the specific wave patterns for these flows can be very similar to the approach suggested by Barthel (Reference 11); however, the flow through the thick grids cannot be considered isentropic. The higher range of incident-wave strengths will produce higher stagnation temperatures in the reservoir region. The longer path through the injector model will encourage heat transfer from the shock-excited gases. The combination of high thermal gradients, convective cooling, and entropy gains caused by friction during flow through the model requires that a nonisentropic approach be considered. Since the relatively steady pressure ratios across the model will be lower than critical, choking is assumed to exist in all cases. This analysis can also be

accomplished on a one-dimensional quasi-steady basis by insuring compatibility of conditions behind the reflected incident wave and entry conditions at the upstream face of the model. It can be similarly accomplished by considering compatibility of final quasi-steady conditions on the downstream face of the model and the state of the gas upstream of the transmitted waves.

Wave Patterns

Since the incident-wave Mach number range is high enough to cause choking at the entrance or exit of the thick-wall grid in all cases, final supersonic regions will appear downstream from the throat of the choked region as a consequence of the sudden downstream expansion. Depending upon the incident-wave strengths, auxiliary left-facing wave systems will be generated in addition to the transmitted wave and contact surface. The conditions upstream of these auxiliary waves must be compatible with the base flows emanating from the perforated plate; the conditions downstream of the auxiliary wave must be compatible with conditions downstream of the transmitted-wave contact surface.

Figure 1 indicates two possible wave patterns expected with a range of incident shock strengths of 4.5 to 29 (i.e., M = 2 to 5). With a primary ratio equal to the breakoff value (or the value at which the streams exhausting from the perforations completely fill the channel), a standing, left-facing auxiliary wave should appear (Reference 14). With additional pressure adjustment in the base region of the plate, the auxiliary transmitted wave will be modified to become a left-facing traveling shock wave (Figure 1a) as reported by Dosanjh (Reference 10) and Barthel (Reference 11). Barthel also speculated on the likelihood of a left-traveling rarefaction wave (Figure 1b) with further increase of incident-wave strength. Although this represents a theoretically compatible condition, this phenomenon was not observed in the experiments he conducted. At the higher range of shock strengths, this should be considered.

Contrary to Barthel's case, with the area ratios under consideration (ϵ = model free area/channel area = 0.25) and the incident-wave Mach number range of 2 to 5, the reflected shock wave will travel

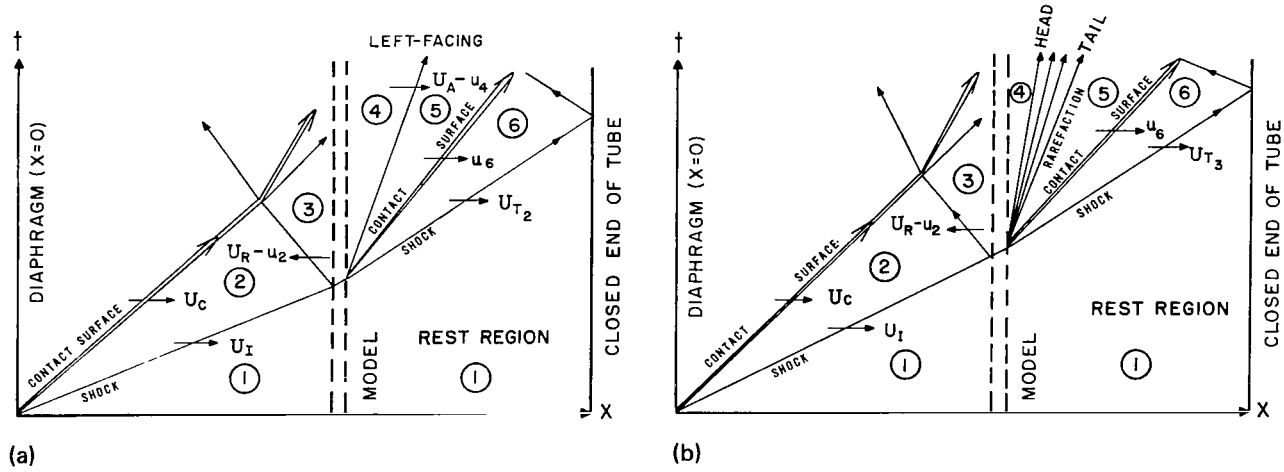

Figure 1—Wave patterns for choked flow through perforated walls. (a) Auxiliary traveling shock. (b) Auxiliary rarefaction wave.

upstream against the drift flow of the incident wave and should increase in velocity as the incident-wave strength is increased. Thus, the reflected wave will not be swept downstream to be stabilized by the perforated plate as occurred in Barthel's work.

The incident wave is assumed to have developed into a plane wave of constant strength by the time it reaches the model since the length of the driven section of the shock tube is several times the minimum specified 10 widths found to be necessary (Reference 15).

Influence Coefficients Method

The incident shock wave, when reflected from the upstream face of the model, will produce a reservoir region of high-pressure, high-temperature gas upstream of the model. The Mach number in this zone will be subsonic with flow directed toward the model. The gas will enter the sharp-edged, cylindrical holes in the model and be subjected simultaneously to cooling and friction.

It is reasonable to assume that a turbulent boundary layer will develop on the walls of the perforations since the reservoir gas has been shocked by both the incident and reflected waves and because the sharp-edged entries of the model perforations act as boundary-layer trips. The transient mixing of shocks and expansions at the upstream face of the model prior to the establishment of steady flow through the model is another contributor to high initial turbulence levels at the entries to model ducts. Analysis of the temperature increase of the model wall during the brief period of relatively steady flow indicated a negligible temperature rise in the perforated plate. This negligible increase and the fact that the plates are made of materials having good thermal conductivity provide a reasonable basis for considering the wall temperatures constant during the testing time.

In the selected range of incident-wave Mach numbers, the passages will choke and therefore determine the entrance Mach number. This entrance velocity will in turn establish the particle velocity downstream of the reflected wave so that compatible quasi-steady conditions can exist in reservoir region 3 of Figure 1.

Shapiro (Reference 16) indicated the general analysis and methods of numerical integration required for the solution of the working differential equations in terms of influence coefficients for generalized one-dimensional steady flow having constant area, constant specific heat, constant molecular weight, constant wall temperature, and combined friction and heat transfer. To simplify the differential equation for heat transfer expressed by means of the energy equation in terms of stagnation enthalpy changes, the following additional assumptions were made: (1) The adiabatic wall temperature T_{aw} does not differ very much from the stagnation temperature T_0; i.e., the recovery factor r is unity; and (2) Reynolds' analogy between friction and heat transfer is valid. These assumptions permit the energy equation to be written as

$$\frac{dT_0}{T_w - T_0} = 2f \frac{dx}{d} , \qquad (1)$$

and the influence coefficients equation becomes

$$dM^2 = F_{T_0} \frac{dT_0}{T_0} + F_f 4f \frac{dx}{d}$$

$$= \left(F_{T_0} + \frac{2T_0}{T_w - T_0} F_f \right) \frac{dT_0}{T_0} \quad . \tag{2}$$

Since T_w is independent of x for a constant wall temperature and considering any pair of sections 1 and 2, integrating Equation 1 yields

$$\frac{1}{2} \frac{4f(x_2 - x_1)}{d} = \ln \frac{T_w - T_{01}}{T_w - T_{02}}$$

$$= \ln \frac{T_w/T_{01} - 1}{T_w/T_{01} - T_{02}/T_{01}} \quad . \tag{3}$$

Thus for any initial value of T_{01} and for selected values of f, d, and T_w, the variation of the stagnation temperature with displacement through the tube or duct can be computed. Equation 2 can then be approximately integrated in a finite difference form over the short interval between incremental sections to provide the variation of Mach number with distance in the duct. The coefficient of dT_0 is assumed constant at its mean value during the interval. $\bar{F}_{T_0}$ and $\bar{F}_f$ denote the values of the influence coefficients when evaluated at $\bar{M} = (M_1 + M_2)/2$ and $\bar{T}_0 = (T_{01} + T_{02})/2$ for the interval. Then the approximate integration for the case of constant wall temperature yields

$$M_2^2 - M_1^2 = 2 \left(\frac{T_{02}}{T_{01}} - 1 \right) \left(\frac{\bar{F}_{T_0}}{T_{02}/T_{01} + 1} + \frac{2\bar{F}_f}{2T_w/T_{01} - T_{02}/T_{01} - 1} \right) \quad . \tag{4}$$

Equation 4 must be solved by iteration since the mean values of the influence coefficients are functions of M_2, which is not known. The value of M_2 must be assumed, used to compute $\bar{F}_{T_0}$ and $\bar{F}_f$, and then solved for in the finite difference equation. This procedure must be repeated for the length of the duct to obtain the distribution of Mach number versus duct length. This is a laborious process for the steady-flow case where upstream conditions are usually known.

In the case for the quasi-steady flows, additional iterations are required which incorporate the above procedure as an intermediate step. The only other useful condition besides the initial conditions is that, at the exits of the ducts, the Mach number of the flow is unity until the transmitted shock reflects from the end of the shock tube and interacts with the drift flow behind the transmitted shock wave. (A thorough discussion of the reasoning for this condition is given in Articles 6.3, 6.4, and 8.9 of Shapiro (Reference 16).) Therefore, to start an iterative process for determining flow conditions before this occurs, a value must be assumed for M_3, the Mach number of the particle flow between the upstream face of the model and the reflected incident shock. (See Figure 2.) The value of M_3 is subsonic and provides A_3/A^* where A^* is the choked area at the exit plane of the duct and A_3 is the upstream channel area.

The first iteration that must be performed is to provide a value for the Mach number of the reflected wave that would be compatible with the assumed value of M_3. The expression to compute

this value is derived in accordance with Shapiro's (Reference 17) analysis of moving shocks in terms of stationary shock formulas:

$$(M_3)_{\text{Reflected wave}} = \frac{M_2 - (M_x)_R}{{}_3C_2 + (M_y)_R} \quad . \tag{5}$$

where $(M_x)_R$ is the initial Mach number of the reflected wave relative to the oncoming flow. $(M_x)_R = U_R/C_2$ is obtained by iteration. This also provides the stagnation conditions in region 3.

$$(A_3/A^*)\epsilon = A_R/A^* \tag{6}$$

where ϵ = plate porosity = A_R/A_3. With the value of A_R/A^* and the isentropic one-dimensional compressible flow tables for $\gamma = 1.4$ (Reference 18), all parameters at the duct entry, point R, can be obtained. The entry Reynolds number based on duct diameter is then computed. Values of the viscosity (Reference 19) at the entry conditions are used for this computation. Knowing the Reynolds number and the L/d ratio for the duct, an estimate of the average friction factor can be obtained (Reference 20) by considering the value at x/d equal to half the incremental length. This estimate is valid because the friction factor versus x/d curve (Figure 3) is linear in this initial region. This enables the computation of the duct-flow longitudinal temperature profile by the use of Equation 3. When the profile is obtained, the successive iterations using Equation 4 are required. If the initial estimate of M_3 was valid, M_E should equal unity; if not, the entire procedure must be repeated until convergence to the desired M_E is obtained.

Limiting Solution Method

It is readily seen that the aforementioned procedure would be very time consuming and complex and that the required additional simplifying assumptions could entail considerable error. An alternate method is proposed, which is based on two individual computations of bounding solutions. The limiting cases should bracket the physical situation, be considerably less laborious, and prove adequate for design purposes. The procedure involves first computing flow through the perforated plate as a duct flow for a Rayleigh process of frictionless flow with a T_0 change, then computing the duct flow for a Fanno process or adiabatic flow with friction. In the case of Rayleigh duct flow, the choked section occurs close to the entry at a vena contracta and supersonic flow exists throughout the length of the duct. In the case of the Fanno duct, the choked section is at the exit plane and subsonic flow occurs for the entire duct length. In both cases, the flow downstream of the perforated plate is supersonic with rapid formation of a base-region flow. When the base-region flows become steady, a relatively stable (constant velocity) downstream contact surface with transmitted primary and auxiliary traveling waves occurs. The Rayleigh bounding solution is called the "lower limit" because its calculations provide lower values of reservoir and transmitted-wave parameters.

Rayleigh Duct-Flow Formulas (Lower-Limit Solution)

The following assumptions are made to analyze the flows for this case. The conditions behind the incident and reflected waves are based on ideal normal shock theory. Real gas properties are used where applicable. The flow behind the reflected wave is compatible with the choked flow at the vena contracta near the entrance of the perforated plate. Downstream of the vena contracta, the flow is

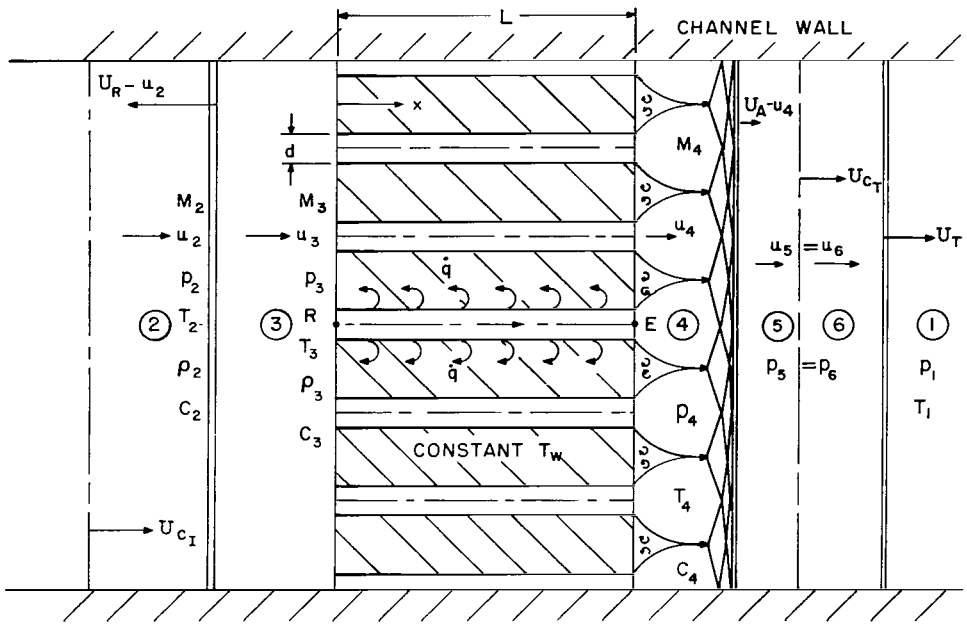

Figure 2—Flow model for thick perforated plate with friction and heat transfer (shown after incident wave reflects from plate).

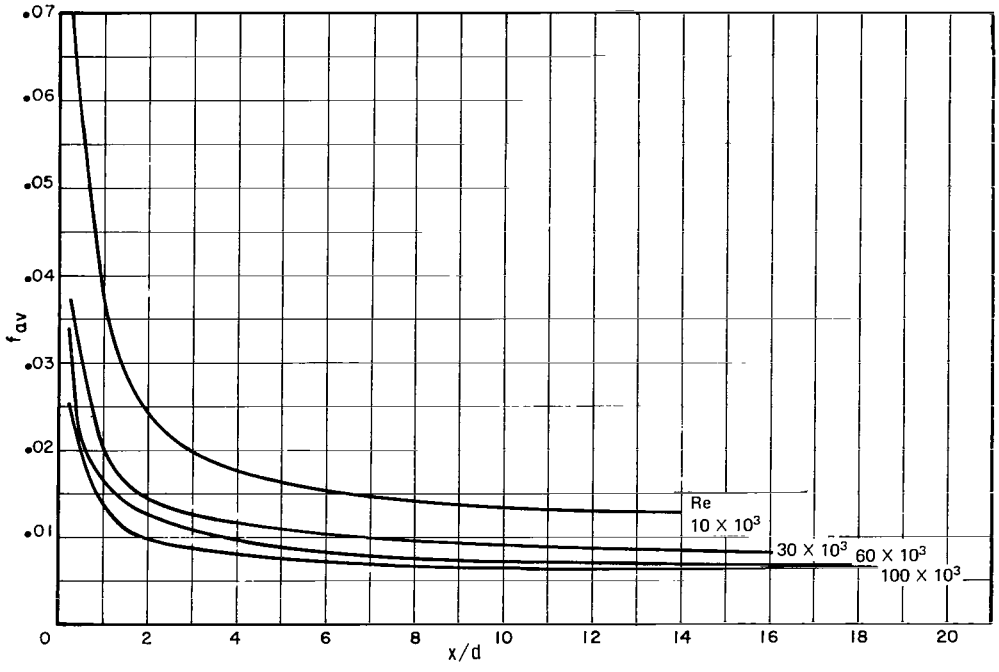

Figure 3—Variation of average friction factor based on static-pressure drop with *x/d* for flow in a tube, constant properties (adapted from Figure 30, Reference 20).

slightly supersonic and in accordance with the isentropic expansion ratio. The vena contracta is assumed to be sufficiently close to the entry plane so that the entire duct can be considered to have supersonic conditions. The experiments performed by Weir and others (Reference 21) have shown this to be essentially the case. It is assumed that the flow through the duct is frictionless and the duct wall is at constant temperature for the brief period of quasi-steady flow. Base region and flows downstream of the model are based upon conservation of mass and momentum and compatibility across the downstream contact surface away from the immediate vicinity of the model.

Upstream Traveling-Wave Formulas

The following equations for traveling waves are required in order to arrive at stagnation conditions for both the Rayleigh duct flow and the Fanno duct flows. They are based on a Galilean transformation (Reference 17) for converting the traveling plane waves in a stationary coordinate system into standing waves in a coordinate system moving at the shock velocity but in the opposite direction.

Therefore, for the conditions behind the incident wave in region 2

$$M_2 = \frac{(M_x)_I}{{}_2C_1} - (M_y)_I \tag{7}$$

where $(M_x)_I = U_I/C_1$ is the incident-wave Mach number and $(M_y)_I$ is the final-state Mach number for a normal shock with initial value equal to $(M_x)_I$.

$$\left.\begin{aligned} p_2 &= \frac{p_y}{p_x} p_1 = {}_y p_x p_1 \,, \\ T_2 &= \frac{T_y}{T_x} T_1 = {}_y T_x T_1 \,, \\ \rho_2 &= \frac{\rho_y}{\rho_x} \rho_1 = {}_y \rho_x \rho_1 \,, \\ p_{02} &= p_2 \left(1 + \frac{\gamma - 1}{2} M_2^2\right)^{\gamma/(\gamma-1)} \,, \\ T_{02} &= T_2 \left(1 + \frac{\gamma - 1}{2} M_2^2\right) \,. \end{aligned}\right\} \tag{8}$$

$$u_2 = M_2 C_2 = M_2 \sqrt{\gamma R T_2 g} \,. \tag{9}$$

The condition of state ratios in terms of initial and final values, x and y, respectively, are obtained from the normal shock tables for $\gamma = 1.4$. Equations 7, 8, and 9 provide all parameters for the flow behind the incident shock for the stationary coordinate system or relative to the shock-tube wall.

The conditions downstream of the reflected incident wave are obtained from Equation 5, where $(M_x)_R = U_R/C_2$. The normal shock relationships hold for the stationary coordinate system as indicated for region 2 in Equation 8.

Flow in the Region of the Perforations

If the Mach number behind the reflected wave is known, the velocity of the reflected wave can be obtained from Equation 5; and with the normal shock tables, the steady-state conditions in the reservoir zone can be computed. However, as shown in Figure 4, the drift flow upstream of the model is controlled by the vena contracta formed at the square-edged entry. The size of this vena contracta can be approximated by considering the empirical work of Koldozie and Van Winkle (Reference 22), who expressed an experimental correlation for the discharge coefficients of thick perforated plates in terms of hole diameter d, hole pitch P, and a coefficient K. Figure 5 shows the hole pattern specified in these terms and also in terms of the parameters considered by Baines and Peterson (Reference 23) and used by Dosanjh (Reference 10). Figure 6 is a plot of the correlation constant K versus thickness to hole diameter ratio for Reynolds numbers up to 20 000. It can be seen that for L/d values over 2.0 the correlation is independent of plate thickness; and, in the Reynolds number range 4000 to 20 000, the correlation is also independent of Reynolds number. Since the models of concern have L/d values of about 10 and Reynolds numbers over 20 000, it can reasonably be assumed that the flat portion of the uppermost curve will closely approximate the steady-state performance of the model for the quasi-steady-state investigation. (In the absence of data for transient studies of C_d, and later heat transfer, data from steady-state experiments were used.) The relationship for the family of curves is

$$(C_d)_{\text{average}} = K\left(\frac{d}{p}\right)^{0.10} . \tag{10}$$

For the model with a $d/P = 0.525$ and $K = 0.98$, $C_d = 0.919$, $A_R/A^* = 1/C_d = 1.0883$, and

$$\frac{A_3}{A^*} = \frac{1}{\epsilon}\frac{A_R}{A^*} = 4.35327 .$$

Both M_3 and M_R are fixed by the above area ratios and the fluid thermodynamic properties. The value of M_3 provides the necessary condition to solve Equation 5 for the reflected-wave speed and sets the reservoir conditions in region 3. The value of M_R provides the entry conditions and the Reynolds number based on diameter. Since real fluid properties are being considered here, iterations must be performed on M_R, γ_R, p_R, and T_R to compute all conditions at R using one-dimensional compressible-flow functions. Tables 7-3, 7-8, and 7-9 of Reference 19 provide additional data required to compute Reynolds and Prandtl numbers for the lower Mach number range. For incident-wave Mach numbers of 4 and higher, equilibrium thermal conductivity values calculated by Yos (Reference 24) are used for obtaining Prandtl numbers.

To obtain a realistic estimate of the T_0 change that occurs in the duct, the following procedure is used. Compute the adiabatic wall temperature

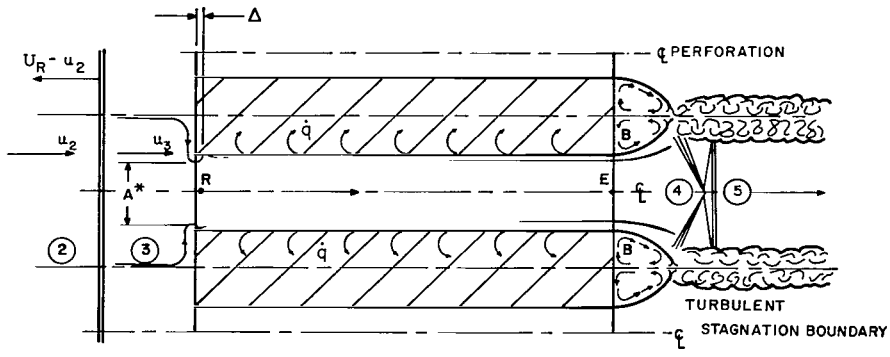

Figure 4—Details of Rayleigh duct-flow model (typical for each individual perforation).

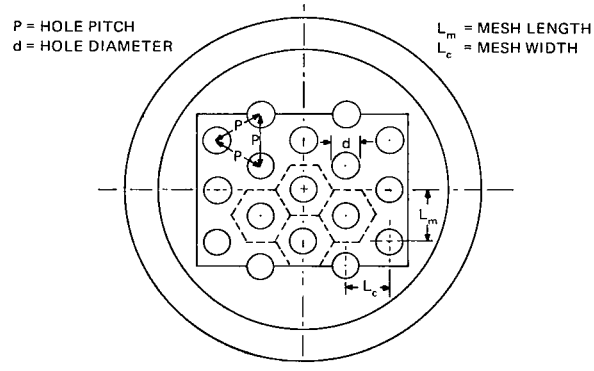

Figure 5—Model hole pattern after Koldozie (Reference 22) and Baines (Reference 23).

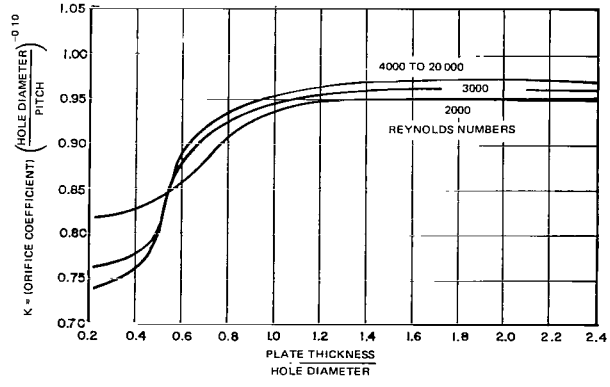

Figure 6—Correlation coefficients for perforated plates versus *L/d* for Reynolds numbers 2000 to 20 000 (Reference 22).

$$T_{aw} = T_R + \sqrt[3]{Pr}\ \frac{u_R^2}{2C_p Jg} \quad . \tag{11}$$

Compute the boundary-layer film temperatures using the static temperature at R for the bulk temperature. This should be close because, at $L/d = 10$, the temperature profiles have not been sufficiently developed to deviate appreciably from the entrance static values. From Reference 20, shown in Figure 7, the value of the parameter X for heat extraction from the gas and

$$T_x = X(T_w - T_R) + T_R \ , \tag{12}$$

where T_w is the initial temperature of the duct wall, provide a datum reference temperature for evaluating the thermal conductivity k_f of the film at the wall. The value of the mean Nusselt number for L/d and the Reynolds number can be obtained from Figure 8. These values enable the determination of an effective heat transfer coefficient to be used in computing the convective heat transfer rate into the wall by means of Equation 13:

$$\dot{q} = h_e A_s (T_w - T_{aw}) \ , \tag{13}$$

where A_s is the surface area of a single duct. The stagnation temperature change can then be computed from the mass flow rate $\rho_R u_R A_R$ and the specific heat at station R:

$$\Delta T_0 = \frac{\dot{q}}{\dot{w} C_p} = 4 \frac{L}{d} \frac{h_e (T_w - T_{aw})}{\rho_R u_R C_p} \quad . \tag{14}$$

The conditions at the exit plane can now be determined by the Rayleigh line relationships for the value of T_0 at E:

$$T_{0E} = T_{0R} - \Delta T_0 \tag{15}$$

Since the isentropic conditions at R are known from $(A_R/A^*)_{\Delta s=0}$, the Rayleigh line unity Mach number parametric values can be computed in terms of the isentropic values and the parametric ratios for the Rayleigh line at the values of M_R. For example,

$$(p^*)_{Ray} = (p_R)_{\Delta s=0} \left(\frac{p^*}{p_R} \right)_{Ray} \quad . \tag{16}$$

An initial value of M_E can be obtained from the stagnation temperature ratio $(T_{0E}/T_0^*)_{Ray}$. Iteration of M_E, γ_E, $(p_E/p^*)_{Ray}$, $(T_E/T^*)_{Ray}$, and the known value of the stagnation temperature ratio determines all conditions at E, the exit plane of the ducts.

Base-Region Flows

Using Wick's relationship (Reference 25) for base pressure to exit-plane pressure ratios in terms of area ratio, exit-plane Mach numbers, and Mach number at the point of reattachment of the expanded flow, Barthel (Reference 11) derived an equation for the base pressure to exit-plane pressure ratio in

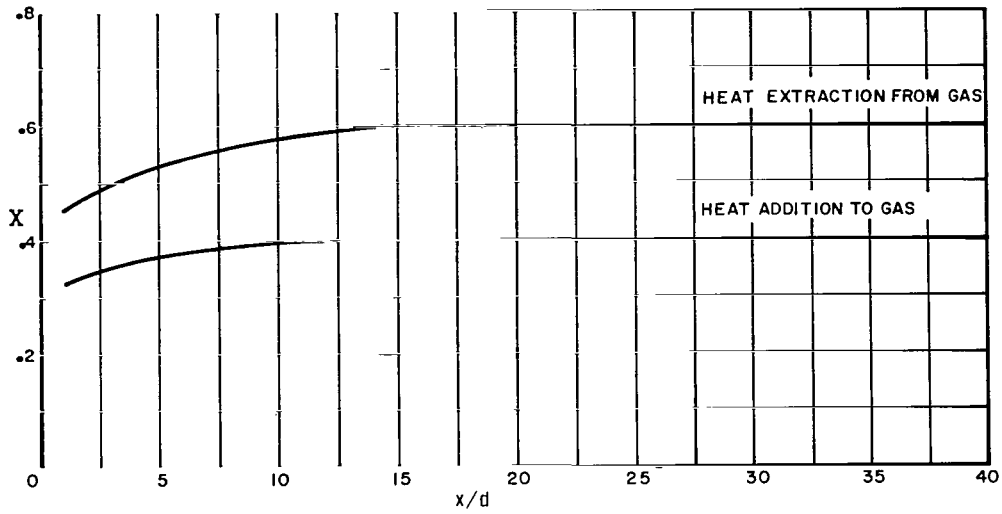

Figure 7—Variation of X with x/d as used in Equation 12 (adapted from Figure 8 of Reference 20).

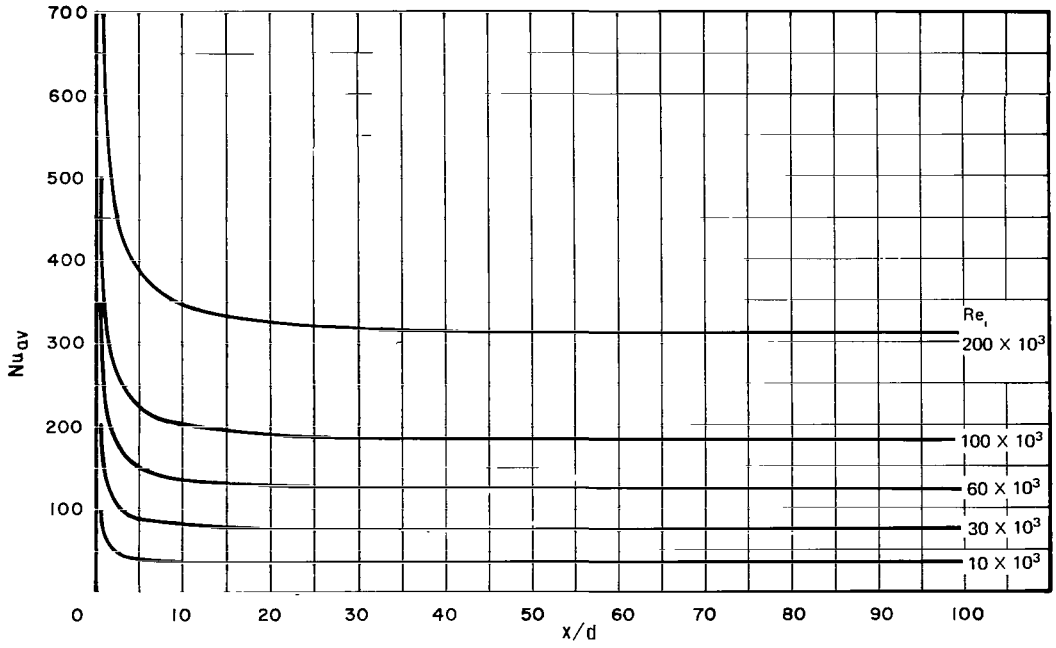

Figure 8—Variation of average Nusselt number with x/d and entry Reynolds number (Re_i) for gas flowing in a tube. Uniform wall temperature, uniform initial velocity, and temperature distributions, and constant properties are assumed (adapted from Figure 24 of Reference 20).

terms of the Fanno line impulse functions at the exit plane and the reattached flow plane for the flow issuing from the ducts into the full channel. Rearranging the equation and using pertinent steady-state experimental base-pressure data presented by Korst (Reference 26) in his work on supersonic axisymmetric internal flows (Figure 9), the impulse function at region 4 (the plane of the reattached expanded flow downstream of the model) can be obtained:

$$\left(\frac{F_4}{F^*}\right)_F = \left(\frac{F_E}{F^*}\right)_F + \frac{1}{\gamma_E + 1}\,\frac{p_B}{p_E}\left(\frac{p_E}{p^*}\right)_F\,\frac{1-\epsilon}{\epsilon} \tag{17}$$

where $p_B/p_E = (p_B/p_{0E})_{\text{Korst}}(p_{0E}/p_E)_{\text{Ray}}$.

Using the value of the impulse function and an estimate of γ_4, the values M_4, p_4, and T_4 can be computed and iterated to check against the impulse function value. Initial estimates of p_4 are obtained from the equation

$$\frac{p_4}{p_E} = \epsilon\left(\frac{p_4/p^*}{p_E/p^*}\right)_{\text{Fanno}} . \tag{18}$$

Initial estimates of T_4 are obtained from the equation

$$T_4 \approx T_E\left(\frac{M_4}{M_E}\,\frac{1}{\epsilon}\,\frac{p_4}{p_E}\right)^2 . \tag{19}$$

Final pressures are computed from the Fanno line pressure ratio, and final temperatures are computed using

$$T_4 = T_E\left(\frac{M_4 p_4}{M_E p_E \epsilon}\right)^2 \frac{\gamma_4}{\gamma_E}\left(\frac{Z_E}{Z_4}\right)^2 \tag{20}$$

Having the conditions in region 4 and the initial conditions of the shock tube, the transmitted-wave patterns can be determined, as shown in the later section, "Downstream Traveling-Wave Formulas."

Fanno Duct-Flow Formulas (Upper-Limit Solution)

Since the computation of the duct flow involving real gas properties requires extensive iteration, the Fanno line solution is based on the gas having a constant $\gamma = 1.4$, and table values for one-dimensional isentropic, normal shock, and Fanno line functions are used (References 18 and 27). For this case, the flow is assumed to be adiabatic and friction is considered in order to determine the entry Mach number M_R that will produce choking at the exit plane E. To start the computation, an initial value of the duct entry Reynolds number must be assumed in order to establish an average value of the friction factor. This provides a value of $4fL/d$ from which the Mach number at R can be obtained using table values of the one-dimensional compressible flow functions for a Fanno line. For the same value of the entry Mach number and the isentropic area ratio corresponding to this number, the isentropic Mach number for the particle flow in region 3 (the stagnation region) can be obtained since

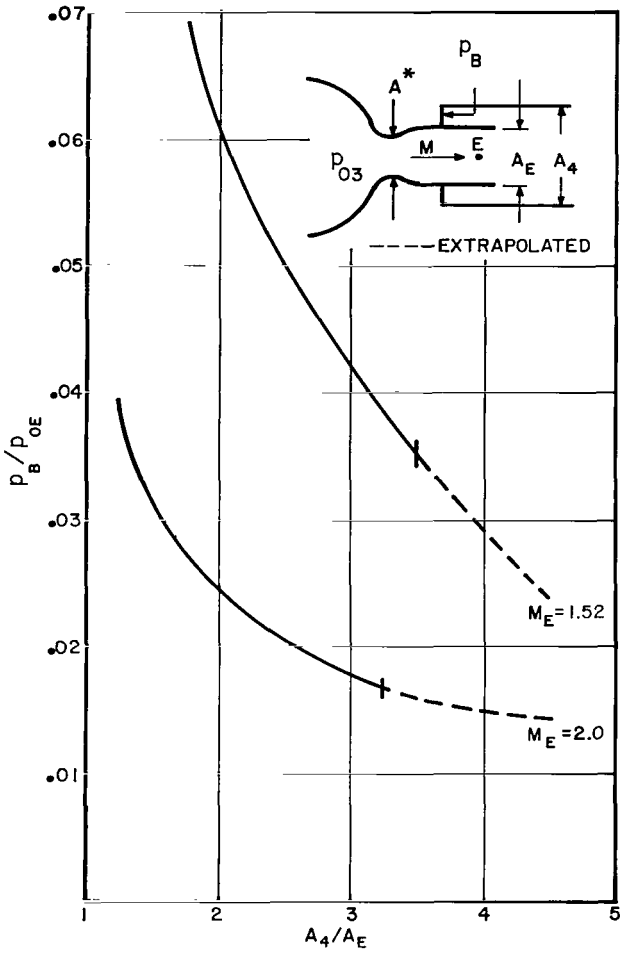

Figure 9—Experimental base-pressure ratios for supersonic axisymmetric internal flow (adapted from Figure 27 of Reference 26).

$$\left(\frac{A_3}{A^*}\right)_{\Delta s=0} = \frac{1}{\epsilon}\left(\frac{A_R}{A^*}\right)_{\Delta s=0} . \tag{21}$$

The value of M_3 corresponding to the resulting area ratio is then fixed for use in the iteration to obtain the reflected-wave speed using Equation 5. As in the case of the Rayleigh duct flow, this establishes the reservoir conditions upstream of the entry and, using data from tables for isentropic, subsonic conditions, all parameters at R can be obtained. The Reynolds number at R can then be computed and checked against the initially assumed value; if it is such that the average friction factors do not change significantly, the original assumption is acceptable. Otherwise, the iteration process must be repeated for the new value of the Reynolds number.

Using Fanno line functions and $M_E = 1$ at the exit plane of the model, all parameters at E can be determined. To determine the conditions in region 4, Kochendorfer's analysis (Reference 14) for a sonic jet expanding into an annular enclosure that is closed at the upstream end and open at the downstream end was used. This analysis assumes a steady adiabatic flow between the sonic exit of the duct and the station at which the sonic jet expands and attaches to the annular enclosure and is directly analogous to the base flows expected during the relatively steady period of the Fanno expansion of the Fanno line solution. From the equations for conservation of mass and momentum, an expression for the Mach number at the plane of reattachment in terms of the porosity ratio of the plate is obtained:

$$\frac{A_E}{A_4} = \epsilon = M_4\sqrt{2(\gamma+1)\left(1+\frac{\gamma-1}{2}M_4^2\right)-\gamma M_4^2} , \tag{22}$$

and the pressure in the same plane in terms of the exit-plane stagnation pressure is obtained:

$$\frac{p_4}{p_{0E}} = \frac{\epsilon\sqrt{[2/(\gamma+1)]^{(\gamma+1)/(\gamma-1)}}}{M_4\sqrt{1+[(\gamma-1)/2]M_4^2}} . \tag{23}$$

This analysis provides the lower limit of the pressure ratio required for the flow to fill the channel and assumes for steady-flow conditions a normal shock at the plane of reattachment. It does not consider entropy losses due to expansion or boundary-layer effects. However, since a thick turbulent boundary layer is assumed to exist and in essence forms a sonic nozzle at the exit plane, the area ratio can be based on exit plane to free channel area or A_4/A^* instead of the geometric area ratio; this provides a slightly higher value of Mach number in region 4. The compatibility of region 4 with the downstream wave patterns can then be determined. For convenience, a plot of area ratio versus region 4 Mach number based on the Kochendorfer analysis is shown in Figure 10.

Downstream Traveling-Wave Formulas

As indicated earlier, there are three possible auxiliary-wave patterns that can be associated with the transmitted shock. The formulas indicated in the following sections will provide the means of establishing compatibility at the transmitted contact surface of conditions in the associated regions.

Auxiliary Left-Facing Standing Shock Wave

At lower incident-wave Mach numbers (on the order of 2 or less), the possibility of an auxiliary left-facing wave should be considered. For this case, the wave should form at or slightly downstream of the point where the base-region boundary stream perimeters intersect and refract. The short region of refraction forms a recompression zone and the complex three-dimensional field rapidly coalesces to form a one-dimensional standing wave. The particle flows on either side travel downstream, and the elevated pressures and temperatures are determined by the normal shock relationships. The upstream Mach number is $(M_x)_A = M_4$, and the Mach number downstream of the standing wave is $(M_y)_A = M_5$. Therefore all conditions at region 5 can be obtained from

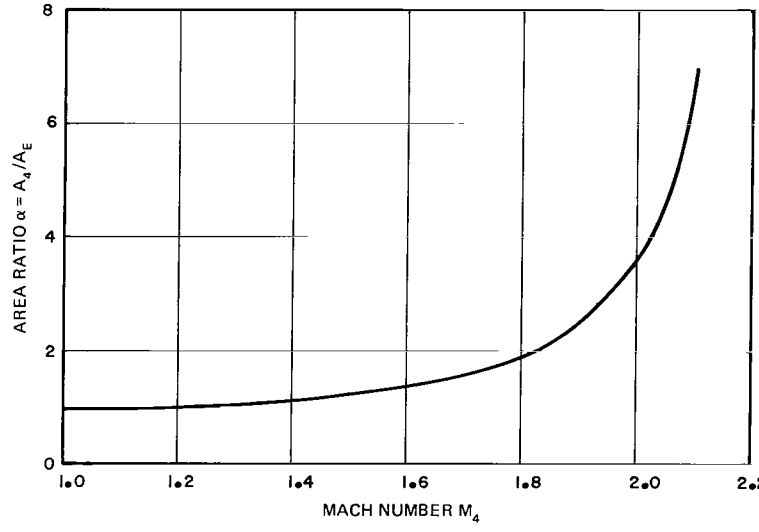

Figure 10—Expansion ratio versus Mach number according to Kochendorfer's analysis (Reference 14).

region 4. Across the contact surface, for quasi-steady conditions, $p_5 = p_6$ and $u_5 = u_6$. These are the compatibility constraints that must be satisfied in determining the speed of the transmitted waves. An iterative process is required to arrive at p_6 and u_6 working back from the region of initial conditions, region 1. If a compatible solution does not exist for the standing wave, a balance will be achieved for some value of M_4 that is different from that determined from base-region considerations.

The region 6 iteration is performed by assuming the Mach number of the transmitted wave $(M_x)_T = U_T/C_1$. The normal shock relationships provide $(M_y)_T$, $p_6 = p_y$, and $T_6 = T_y$ since $p_1 = p_x$ and $T_1 = T_x$. By transforming the coordinate system from a stationary one to one moving at the transmitted shock velocity, an expression for particle velocity u_6 is obtained:

$$u_6 = (M_x)_T C_1 - (M_y)_T C_6 \ . \tag{24}$$

The existence of the auxiliary standing wave can then be tested.

Auxiliary Left-Facing Traveling Shock Wave

The left-facing auxiliary traveling wave is the most likely to satisfy the transmitted contact surface compatibility constraints for this incident-wave Mach number range, and its existence has been experimentally verified by several investigators. The wave, although left-facing, will travel downstream with reference to a stationary coordinate system at the velocity $U_A - u_4$ and its rate will increase with an increase in incident-wave strength.

The value of M_5 in this case is obtained by assuming the value of $(M_x)_A = U_A/C_4$ and using the relationship

$$M_5 = \frac{M_4 - (M_x)_A}{{}_5C_4} + (M_y)_A \ . \tag{25}$$

Using the normal shock relationships, $p_5 = {}_y p_x p_4$, $T_5 = {}_y T_x T_4$, ${}_5C_4 = \sqrt{{}_y T_x}$, and $u_5 = M_5 C_5$. Since $p_5 = p_6$, p_6/p_1 determines the Mach number of the transmitted wave. By means of the normal shock relationships and the initial conditions, all parameters in region 6 can be computed. The particle velocity in this region, u_6, can then be computed using Equation 24. If u_6 is larger than u_5, a smaller value of $(M_x)_A$ is assumed and vice versa until u_5 checks u_6 within 1 percent.

Auxiliary Left-Facing Rarefaction Wave

Barthel (Reference 11) suggested the possibility of the formation of a transmitted auxiliary rarefaction wave as incident-wave strengths are increased. His reasoning was based on the gradual lowering of velocity of the left-facing auxiliary shock as incident-wave strength increased. Assuming the velocity was sufficiently lowered so that the auxiliary shock strength approached a sound wave, this possibility could follow. However, he did not experience this in the low Mach number range that was tested. It is doubtful that this will occur even at higher incident-wave Mach numbers, since analysis predicts appreciably higher wave strengths for a rarefaction wave then it does for an auxiliary traveling shock wave which should not occur with sound waves.

This analysis was based on relationships between sound speed and pressure at a rarefaction wave and on maintaining compatibility at the transmitted contact surface. Again an iterative process is required to utilize the fundamental equations. A value of p_5 must be assumed to compute the sound speed in region 5. Since motion of sound waves is isentropic, the Mach number in the region can be computed using the stagnation pressure of region 4. The sound speed and Mach number provide the particle velocity in the region, which must be balanced against the particle velocity of region 6 as computed in the previous section. The equations required are as follows:

$$C_5 = C_4 \left(\frac{p_5}{p_4}\right)^{(\gamma-1)/2\gamma} \tag{26}$$

$$p_{04} = p_4 \left(1 + \frac{\gamma - 1}{2} M_4^2\right)^{\gamma/(\gamma-1)} \tag{27}$$

$$M_5 = \sqrt{\frac{2}{\gamma - 1}\left[\left(\frac{p_{04}}{p_5}\right)^{(\gamma-1)/\gamma} - 1\right]} \,. \tag{28}$$

The pressure in region 5 must balance the pressure in region 6. Therefore, the primary transmitted-wave shock strength is specified and all parameters in region 6 can be computed based on the initial conditions of region 1. The particle velocity u_6 computed from Equation 24 must equal u_5 or the iteration must be carried further.

The numerical results from the computations described in the preceding sections are presented and discussed later.

APPARATUS AND EXPERIMENTAL PROCEDURE

To assess the correlation of the theoretical calculations with actual flow behavior, an experimental program was conducted. A shock tube was designed to generate plane traveling waves in the range of incident-wave strengths previously discussed. Particular attention was paid to surface finish, surface discontinuities, rigidity, and instrumentation capability. This section describes in detail the basic facility and its instrumentation, the models used, and the test procedure.

Shock-Tube Design

The shock tube, Figure 11, is a high-strength, thick-walled, rectangular steel box of uniform cross section having inside dimensions of 1.50 in. high by 2.00 in. wide. The first-stage helium driver section consists of two 24-in.-long flanged units bolted to make up a 48-in.-long reservoir. If required, a third 24-in.-long unit can be inserted to provide a 72-in. driver. The second-stage driver is a flangeless unit 2 in. long and is clamped by four massive C-bars between the first-stage driver and the driven section. Two identical pure aluminum diaphragms are interposed between the 2-in. section and the clamping flanges. The nitrogen-filled driven section consists of five 24-in.-long flanged units. The

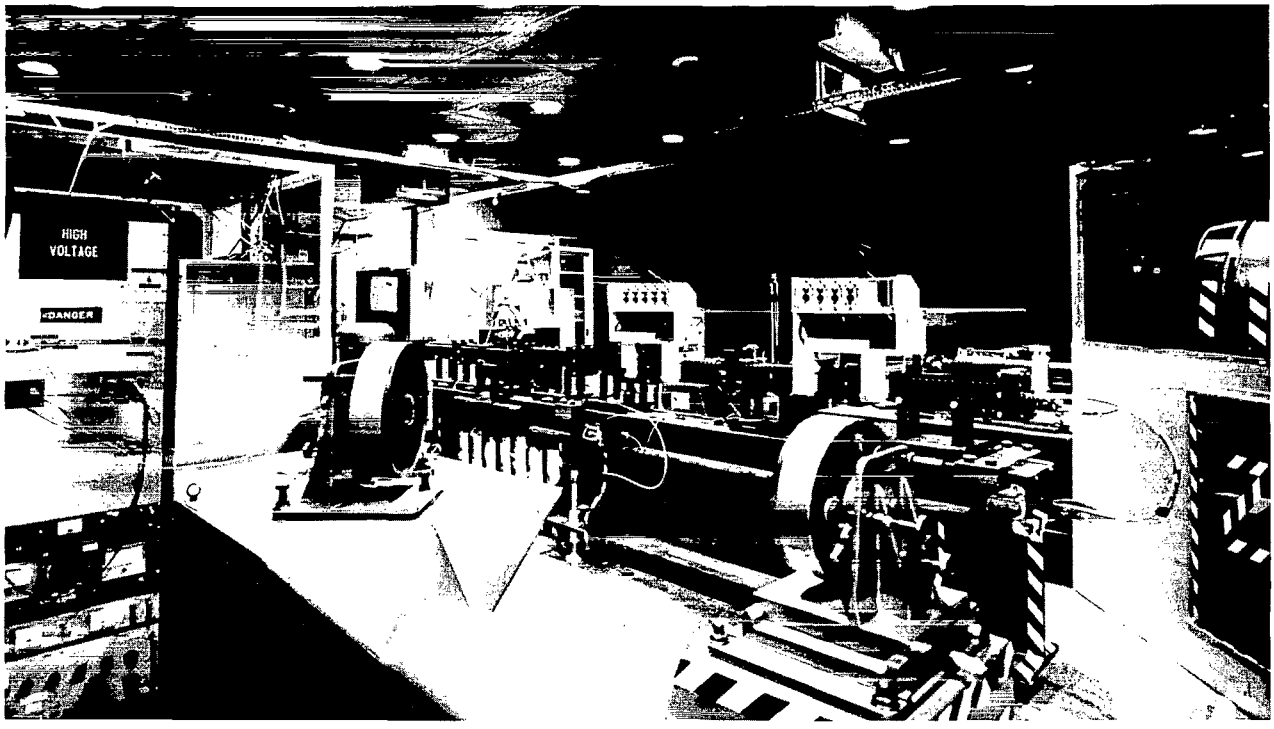

Figure 11—Overall view of shock-tube laboratory.

model injector plates are clamped between the third and fourth units, which have 10-in.-long full-height glass or plastic windows adjacent to the model faces to enable optical recording of interaction phenomena. Since the incident wave can travel 72 in. prior to impinging on the face of the model, it should have ample time to develop a uniform strength across the tube cross section. The proportioning of the basic tube and the detail design was in accordance with generally accepted practice (References 28 to 30).

The double diaphragm arrangement is used in conjunction with cruciform-milled aluminum plates to eliminate the need for diaphragm piercers. The 2-in. section is pumped to about one-half the pressure of the first-stage driver. When the pressure of the 2-in. section is exhausted to atmospheric pressure by means of a solenoid valve, the upstream diaphragm ruptures and dumps the full pressure on the downstream diaphragm. The downstream diaphragm then rapidly ruptures with minimal deformation because of the higher loading rate. The diaphragms petal cleanly without tearing and the repeatability of the breaking load can be kept within 5 percent on properly fabricated units.

All major shock-tube parts are made of heat-treated SAE 4150 steel plates that were machined and ground to size and have at least an 8-μin. rms internal finish. The plates are electrodeless, nickel plated, and electroblackened to provide a hard corrosion-resistant dull coating on the surfaces. The plates and flanges were assembled with high-strength bolts and dowels. The assembled sections are supported on individual carriages which permit lateral positioning. The carriages roll on hardened and ground guide rods by means of chain-linked roller bearings. The guide rods rest in V-grooves milled

into the rigid structural steel base; the base is mounted on heavy-duty swivel casters and jacks for portability and positioning. Instrument ports are located in the top and bottom plates of all sections. They are ½ in. in diameter and are filled by O-ring sealed plugs mounted flush with the inside wall. All temperature and pressure measuring instrumentation is inserted into the system by means of these ports.

The upstream and downstream test sections are similar in construction to the other units except that thick fused-silica or cast acrylic windows (optically flat) provide a clear view of the interior of the flow channel 10 in. in either direction from the faces of the model when it is clamped between the two test sections. There are instrument ports every 2 in. starting at the model face for the first foot of length in the top and bottom plates. These provide a flexible arrangement for tranducer location and for triggering auxiliary electronic circuitry. Fiducial wire grids clamped outside the glass windows provide a convenient scale of reference for optical determinations of wave speeds. Massive T-bars, shown in Figure 12, restrain the cantilevered ends of the upper and lower plates at the model faces. This is necessary in order to provide the support lost by having a split clamp flange at the model faces; the flange was split to offer an unobstructed view of the model-gas interface.

The shock tube is manifolded to vacuum pumps and to nitrogen and helium supplies by means of a graphic control panel. The panel controls enable the evacuation of all three sections of the shock tube, pressurization of the driver sections using either an 800- or a 3500-psi helium supply, and pressurization of the driven section using a low-pressure (80-psi maximum) nitrogen supply. The panel

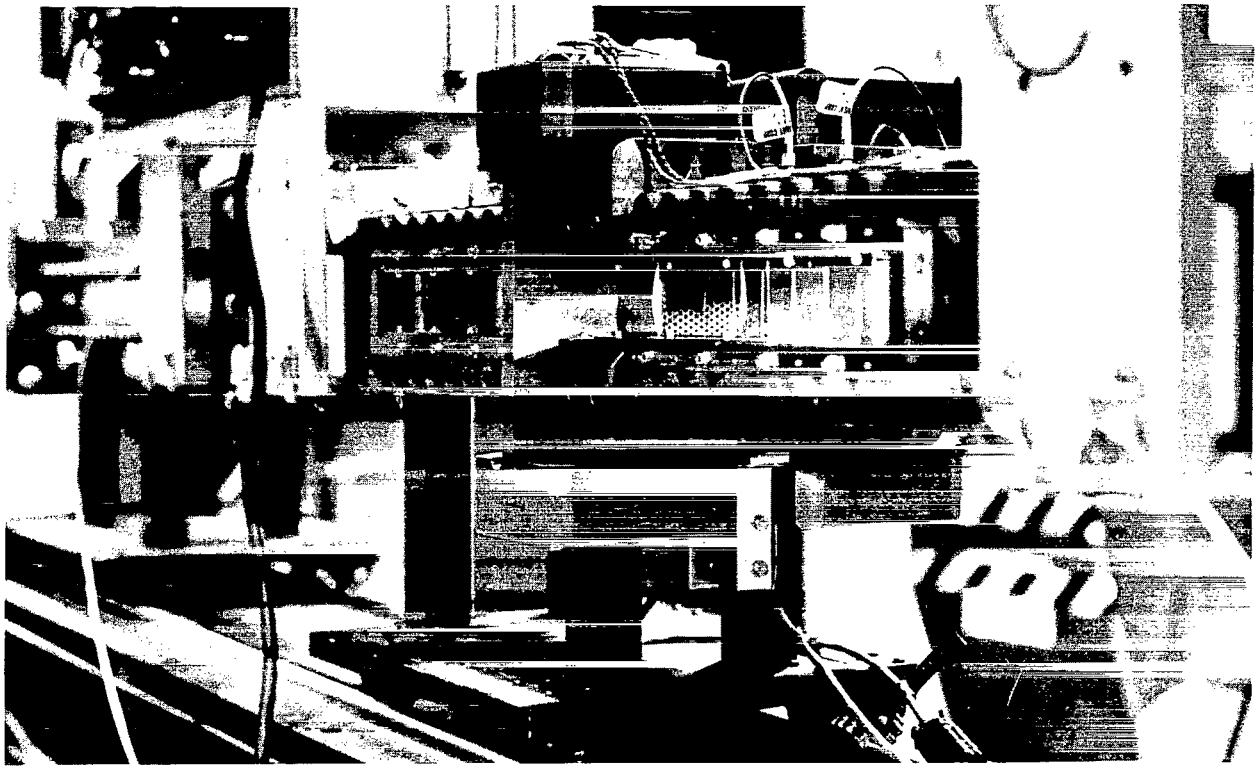

Figure 12—View of test section showing split flanges, T-bars, model, fiducial grids, and instrumentation.

contains master gages for indicating vacuum and pressures for system scavenging and charging purposes. The gages and supply lines are piped to permit in-line calibration with primary and secondary standards.

The gases are supplied from bottle banks and cleaned by passing through purifier units prior to regulation. The higher pressure helium is obtained by boosting gas regulated at 800 psi to 3500 psi in a diaphragm compressor and storing in high-pressure receivers (1772 $in.^3$). The shock tube can be pumped down to 0.1-mm-Hg pressure in less than 10 min using a small two-stage vented-exhaust vacuum pump rated at 140 liters/min. For higher pumping rates, it can be manifolded to two tandem-arranged vacuum pumps each having a nominal rating of 1600 ft^3/min.

Instrumentation

The instrumentation used with the facility can be categorized as either steady-state or transient measuring systems. The steady-state instruments include those required to establish initial conditions in the shock tube. The transient measuring systems are those that provide the data required to assess interaction phenomena produced when the generated traveling waves impinge on the model faces.

Steady-State Measurements

The steady-state measurements of pressure in the various sections of the shock tube are made with solid-front, temperature-compensated units. The vacuum that scavenges the system prior to each run is measured by an 8½-in. 0- to 760-mm-Hg (1-mm-Hg divisions) gage using ambient pressure as the datum point. This same gage is also used to measure the low pressure to which the nitrogen-filled driven section is charged. To monitor the driven section pressure when the more precise vacuum gage is valved off, a 6-in. 0- to 1000-psi (1-psi divisions) absolute pressure gage is connected to the driven section supply line.

Two 8½-in. gages are manifolded to each driver section to cover the complete range of charging pressures. The short second-stage driver is measured by 0- to 250-psi (0.5-psi divisions) and 0- to 2500-psi (5-psi divisions) units; the long first-stage driver is measured by 0- to 500-psi (1-psi divisions) and 0- to 5000-psi (10-psi divisions) units. High-pressure hand valves enable the selection of the gages suitable for the test pressure levels.

The initial temperature of the gas at rest is assumed to be the same as that temperature monitored within the channel wall at a distance of 0.061 in. from the interior surface. This assumption is reasonable since adequate care is taken to insure that the equilibrium wall temperatures are close to ambient conditions; the small volumes of gas within the channel should quickly stabilize to the wall temperatures. Type K (chromel-alumel) welded thermocouples are located in four instrument plugs at stations 37, 60, 116, and 10D of the tube. Two additional thermocouples are inserted into the model. The thermocouple extension leads are terminated at a thermoelectric manual-switching unit which enables the selection of a single output for display on a digital thermocouple indicator. When all temperature channels agree within 1 F°, the channel is considered to be at thermal equilibrium and ready for a test run. Figure 13 is a view of the control panel and the digital temperature-indicating system.

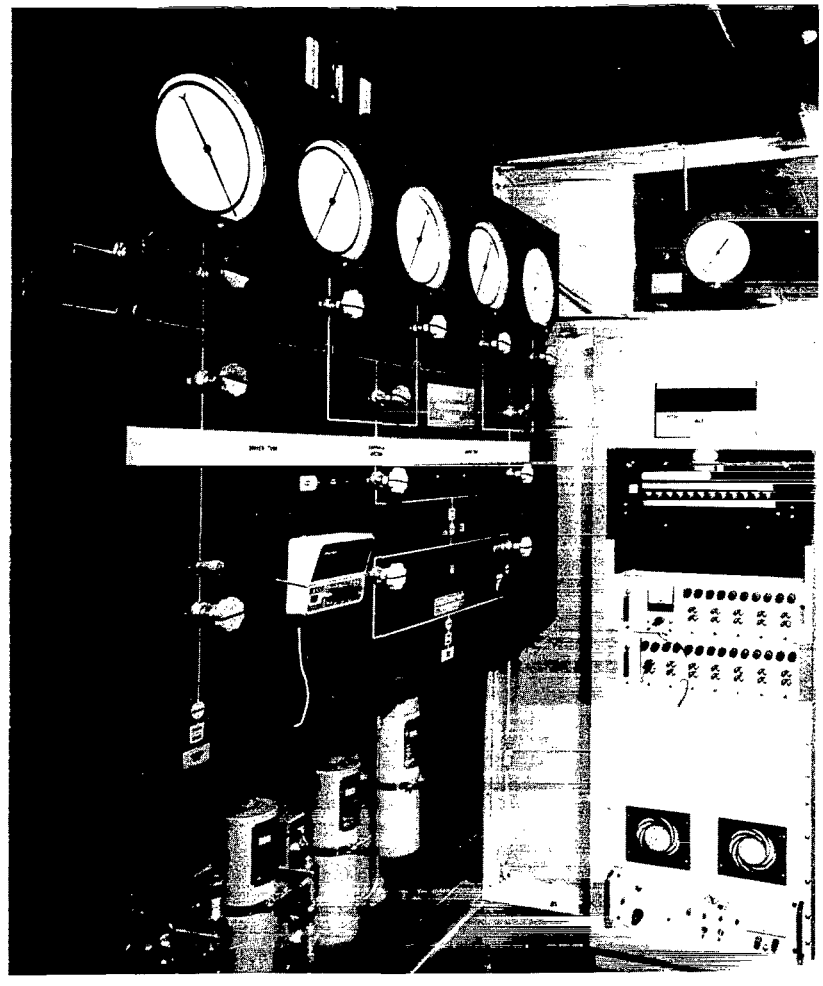

Figure 13–Shock-tube pressure control panel and digital temperature-indicating system.

Transient-State Measurements

Three major modes of data acquisition are utilized to measure the flow fields prior to and during interaction with the models. They are

(1) High-response pressure transducers to acquire pressure histories

(2) High-speed electronic counters to measure average wave speeds at discreet positions in the tube

(3) High-speed framing camera to provide a wave-speed history for a distance of 10 in. upstream and downstream of the model and to photographically record interaction phenomena

High-Response Pressure-Measuring System

The components of the pressure-measuring system include quartz pressure transducers having a nominal sensitivity of 0.35 pCb/psi and a resonant frequency greater than 400 000 Hz. The transducer is flush mounted into the shock-tube wall by means of a brass instrument port plug machined to accept the transducer, its metallic seal, and its connector adaptor. The brass plug is retained by a 5/8-18 UNF thread at the outer wall surface, but is sealed at the inner wall by an O-ring on its 0.500-in. diameter. The charge signals generated by the shock pressure steps are converted into low-impedance voltage signals compatible with cathode-ray oscilloscopes by means of electrostatic charge amplifiers. Two channels upstream and two channels downstream of the model are used to record pressure histories. The oscilloscopes are wide-range dual-beam units providing a frequency capability in the DC to 30-MHz range. They permit individual or synchronized control of the time base plug-in units; the vertical channels utilize separate plug-in preamplifiers. The upper beam preamplifier is a fast-rise, high-gain unit with a deflection capability of 5 mV/cm to 20 V/cm having a passband of DC to 30 MHz and a rise time of 12 ns; a square wave is fed into this channel by a pulse generator to provide a voltage and frequency calibration signal for data reduction of the lower-beam pressure traces. The lower-beam plug-in preamplifier is a four-trace unit having a DC to 20-MHz passband and an 18-ns rise time, with a deflection factor of 0.02 to 10 V/cm. The two pressure transducers on the upstream side of the model use the first two channels of this preamplifier in the chopped mode of operation. An identical arrangement exists for the two pressure channels on the downstream side of the model with a second oscilloscope whose upper beam is also linked to the calibration pulse generator.

A total of nine pressure transducers is distributed along the length of the shock tube. In addition to the four transducers that provide pressure histories and trigger complementary instrumentation, five other units are used for triggering purposes only. Figure 14 shows the transducer installations and the close-coupled charge amplifier racks. Figure 15 schematically indicates the overall instrumentation arrangement.

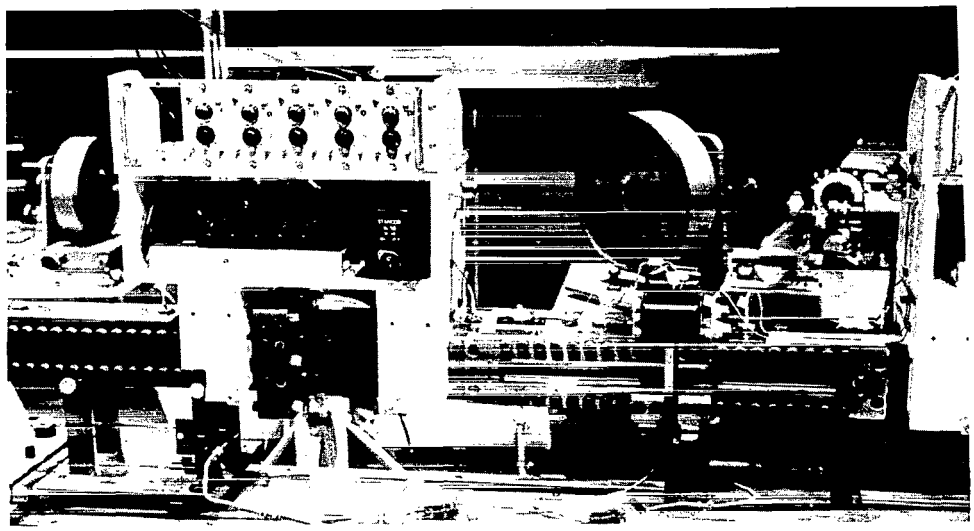

Figure 14—Pressure transducer and charge amplifier installation for data acquisition and triggering functions.

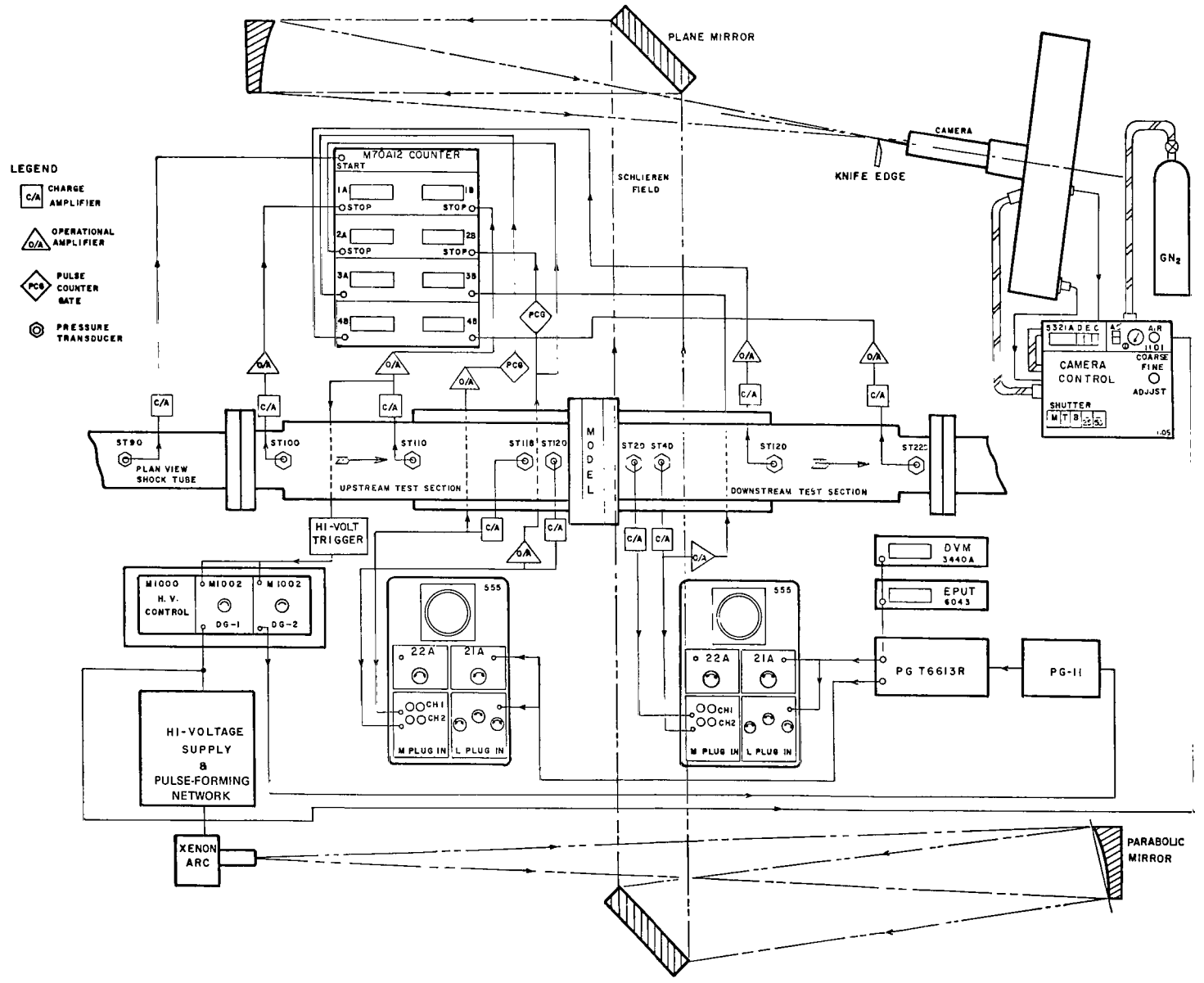

Figure 15—Layout of dynamic data acquisition system (no scale).

Wave-Speed Measurement

The average wave speeds are measured in selected locations upstream and downstream from the model. The incident-wave speed is averaged over a 10-in. interval 12 in. and 2 in. upstream of the model. The reflected-wave speed is measured over a 2-in. interval 2 in. upstream of the model. The transmitted-wave speeds are measured over an 8-in. interval 2 in. downstream from the model and over a 10-in. interval 12 in. downstream from the model.

The time intervals for traversing these distances are recorded on a multichannel counter. This counter system has two master clocks, a common master start, individual stops, individual resets, and master reset capability. The clock frequency is 10 MHz with a minimum timing capability of 0.3 μs. The counters are started when the incident wave excites the transducer at station 90, which is 32 in. upstream of the model. The transducer signal is amplified by the charge amplifier and then fed directly to the start input of the counter bank. The charge amplifier range is set to produce about a 1-V signal at each incident-wave speed for reliable triggering. The stop circuits have additional auxiliary electronics since the other charge amplifiers are set at only one range and are not changed. This is done to avoid a variable response due to the effect of amplifier feedback capacitance on unit time constant and to match amplifier delays. To provide the additional amplification for triggering on these channels, the outputs of the charge amplifiers are fed into low-gain, high-response operational amplifiers ($\mu \approx 20$) and the outputs of these are then used to trigger the counter channels that monitor downstream traveling-wave speeds. To measure the reflected-wave speeds (upstream traveling), the outputs of the operational amplifiers at stations 118 and 120 (4 in. and 2 in., respectively, upstream of the model) are fed to pulse-counter circuits that provide a fixed output to the counter gates when the second-higher-level pressure pulse of the reflected wave triggers these units. Figure 16 shows the rack containing the counter system, the triggering and gating unit (the pulse counters), and the conditioner unit (operational amplifiers).

Having direct digital indication of incremental elapsed time from the counter bank and the incremental distances between transducer stations, the average wave speeds can be readily determined.

Optical Instrumentation

The optical recording system consists of an $f/8$ folded Z-type schlieren system, two pairs of optical flats in the vertical walls of the shock-tube test section, appropriate light sources, and a continuous writing streak and framing camera. The schlieren components are supported on two massive (1400-lb) pedestals that are aligned parallel to the shock tube. They include off-axis parabolas and produce a fully collimated 10-in.-diameter working beam that is perpendicular to the shock-tube longitudinal axis. The shock tube is illuminated by arc lamps in the vicinity of the optically flat windows of the test sections. Since the flow channel is mounted on movable carriages, it can be positioned so that the upstream window, injector plate model, or downstream window are centered in the working beam. The 1.5-in.-high by 10-in.-long glass windows and mirror system components are diffraction limited (ground and polished to within one-tenth the wavelength of green light, 5400Å). The off-axis angle of the fused silica parabolas is less than 7°. The steady-state light source used for alignment purposes is a mercury-vapor unit. High-pressure 80-W short-arc xenon flash lamps are used for short-duration illumination exposures for the camera. They are energized by inductance-

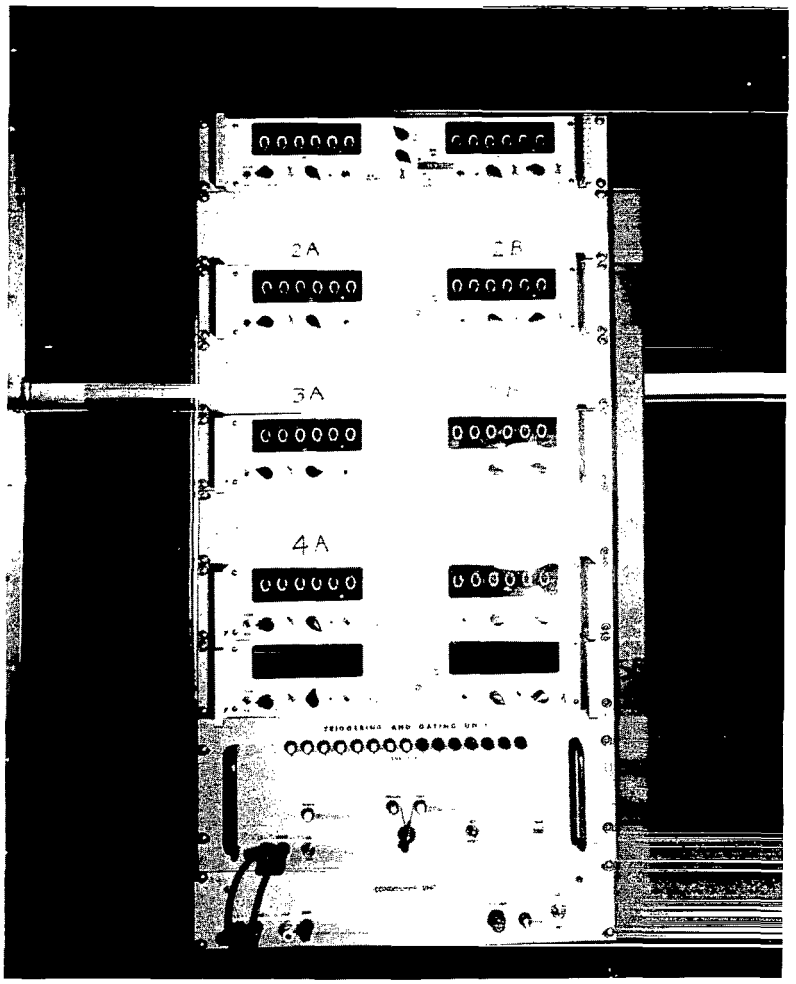

Figure 16—Wave-speed measuring system consisting of chronograph units, operational amplifiers, and pulse-counting gating unit.

capacitance pulse-forming networks, similar to those described by Mauldin and Compton (Reference 31), to produce square wave pulses of light having durations of 100, 400, and 1200 μs.

The camera system, modified to run at 12 000 to 2 000 000 frames per second, is used in conjunction with an auxiliary field lens assembly (Figure 17) so that the field of view is about 10 in. in diameter to match the working beam size. The 35-mm format provides a nominal frame size of 16 by 25 mm. With the 360-mm-focal-length objective lens set at infinity, the 10-in. field should completely fill the frame. The rotating mirror turbine is driven at a rate compatible with the selected light pulse duration to prevent overwriting on the two 40-frame film strips that comprise the record of a single run.

The light source is triggered by the output of the pressure transducer located 12 in. upstream from the model (station 110). The transducer charge is converted to a voltage signal in the charge amplifier and then fed to the high-voltage trigger unit which provides a 200-V maximum negative

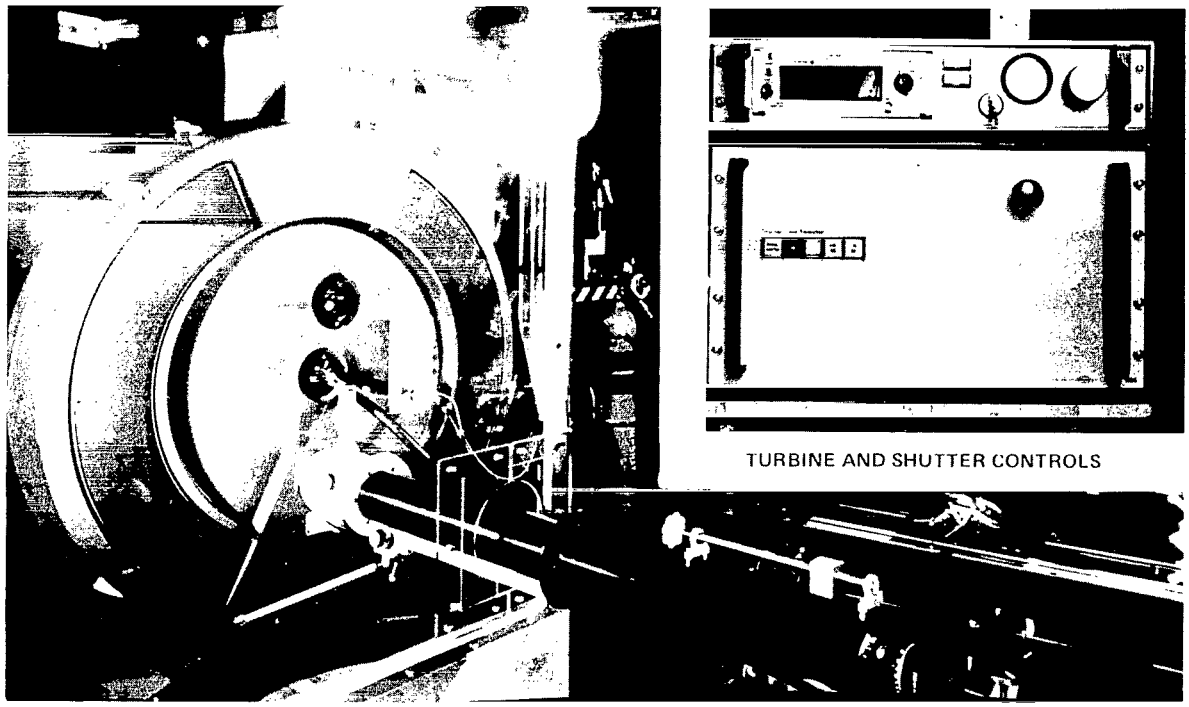

Figure 17—The continuous streak and framing camera system (camera turbine and shutter controls shown at inset).

step output. The negative step triggers the first channel of a two-channel delay generator unit. The delay generator output is a positive pulse of 250 V; it is used to trigger the light-source power supply and the camera turbine air cutoff control. The output of the high-voltage trigger unit is also fed into the second channel of the delay generator console. The output of this second channel triggers the square wave pulse generator (frequency and voltage calibration signal) that is fed to the oscilloscope preamplifiers, which in turn triggers the sweeps of the two oscilloscopes that record the pressure traces on positive photographs.

The 35-mm film strips provide data on wave speeds, wave acceleration, and a photographic record of the flow-field development. When examined with the pressure traces, they provide a complete history of the transient interaction phenomena.

Kodak Plus-X Pan 35-mm film was used for all pictures and the developer was Diafine dual bath with a developing cycle of 10 min in bath A and 6 min in bath B at 70° F.

Test Configuration

As indicated in the discussion of the shock-tube design, the models are in the form of plates that are clamped between the split flanges of the upstream and downstream test sections. An 0.030-in.-thick rubber gasket is seated around the 0.080-in.-high by 1.50-in. by 2.00-in. boss on each model face. This provides a vacuum-tight seal between the models and the test section faces when properly assembled and bolted. Dowels inserted into the ends of the horizontal plates of the test sections

provide alignment of the models and the shock tube. The models, shown in Figure 18, are machined from aluminum alloy 2024-T4. The hole patterns were produced by precision drilling, reaming, and lapping to size. Edges were maintained square and sharp by grinding and lapping the faces of the plates.

Two models were considered for the experimental program. Both have nominal L/d values of 10 and porosity factors of 0.25. The hole sizes were selected to provide a hole area scaling factor of 10 to 1 between models. One model has 179 effective passages of 0.078 in. in diameter by 0.875 in. long resulting in an L/d value of 11.15; the other model has 17 effective holes 0.250 in. in diameter by 2.500 in. long with L/d equal to exactly 10. Thermocouple wells drilled from the top surface enable measurement of the model temperatures on the vertical centerline to within 0.060 in. of the uppermost flow passage. The wells are located 0.187 in. from the model faces on the 0.875-in.-thick model and 0.500 in. from the faces of the 2.500-in.-thick model. Number 30 AWG chromel-alumel thermocouples mounted on slotted 0.125-in.-diameter Micarta rods are fitted to the wells so that their hot junctions make intimate contact with the flat bottoms of the wells.

Test Programs

For each model, experiments were run for selected positions of the model relative to the schlieren beam with the incident-wave Mach number varied over the nominal range of 2 to 4.6. To test over this wide range of Mach number with maximum safety, cast acrylic windows were used instead of the glass. Since it was not feasible to polish the plastic to the flatness of glass, there was a resulting loss of resolution at the faces of the model due to edge diffraction.

The initial position presented the flow field of the incident and reflected waves at the upstream model face; the second position centered the model in the schlieren beam to show upstream and

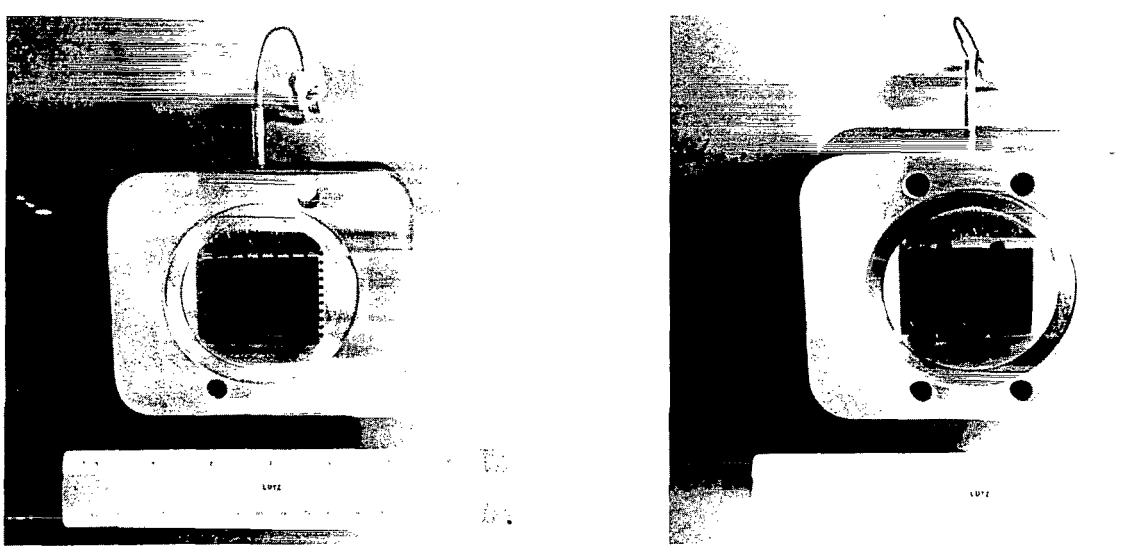

(a) (b)

Figure 18—Aluminum models with $\epsilon = 0.25$ and $L/d = 10$. (a) $d = 0.078$ in. (b) $d = 0.250$ in.

downstream fields in close proximity to the model; the third position permitted examination of the transmitted-wave patterns downstream of the model face. A minimum of four values of incident-wave Mach number were tested in the designated nominal range. At each value of Mach number, five repetitive tests were performed to assess variability. Schlieren beam position was varied to obtain optimal data. In general, initial conditions, counter-wave-speed data, pressure transducer output, and high-speed photographic records of the various flow fields were acquired for each of the test runs in the ranges Mach 2 to 4.6 for the 0.078-in.-hole-diameter and Mach 2 to 3.75 for the 0.250-in.-hole-diameter model. Thus for a full range of tests for each model, 20 to 25 runs were performed.

Experimental Procedure

The following is a description of the sequential operations that were used to perform a single test run with the 1.5- by 2.0-in. shock tube.

The selected model was clamped between the test sections and a leak test was performed to guarantee that the assembly was within tolerance; i.e., 5-mm-Hg maximum pressure rise in 15 min after evacuation to less than 1-mm-Hg absolute pressure.

The amplitude and frequency of the pulse generator output was adjusted to selected values using secondary standards. The oscilloscope time base and amplification ranges were set using the calibrated output of the pulse generator. Counter attenuations were set and counter "start" trigger levels were adjusted.

Shock-tube and model temperatures were permitted to stabilize to within 1 F° of ambient and recorded. Vacuum and pressure gages were zeroed. The appropriately sized diaphragms were seated at both faces of the 2-in. driver section with stress grooves facing downstream, and the assembly was clamped into the shock tube using the C-bars (Figure 19). Bolt torques were kept lower than 90 percent of the maximum allowed. The driver and driven sections were evacuated until the vacuum gage varied from the ambient barometric pressure by less than 0.5 mm Hg. The driven section was then charged with dry, filtered nitrogen (dewpoint, -98° F) to a pressure of 5 psi absolute. The two driver sections were brought up to the pressure required for the 2-in.-long section using dry, filtered helium. Finally, the first-stage driver was brought to full pressure.

The framing camera was loaded with film strip from the cassette loader magazines; the camera turbine speed was adjusted to correspond to the duration of the selected arc lamp flash. The transducer charge amplifiers were grounded, oscilloscope sweeps reset, counters reset, and delay generators reset. The room lights were turned off and shutters of the framing and oscilloscope cameras opened. The solenoid dump-valve push-button switch was operated. The scope camera shutters were closed, the room lights were then turned on, and the framing camera strips retrieved into the cassettes for processing. Counter readings were recorded. Oscilloscope records were removed and properly annotated with run number, incident-wave Mach number, model number, beam position, and pulse generator input wave amplitude and frequency.

DISCUSSION OF RESULTS

The following discussion deals with the results of the theoretical consideration of the Rayleigh and Fanno flow models in terms of the compatibility of the three possible auxiliary-wave patterns

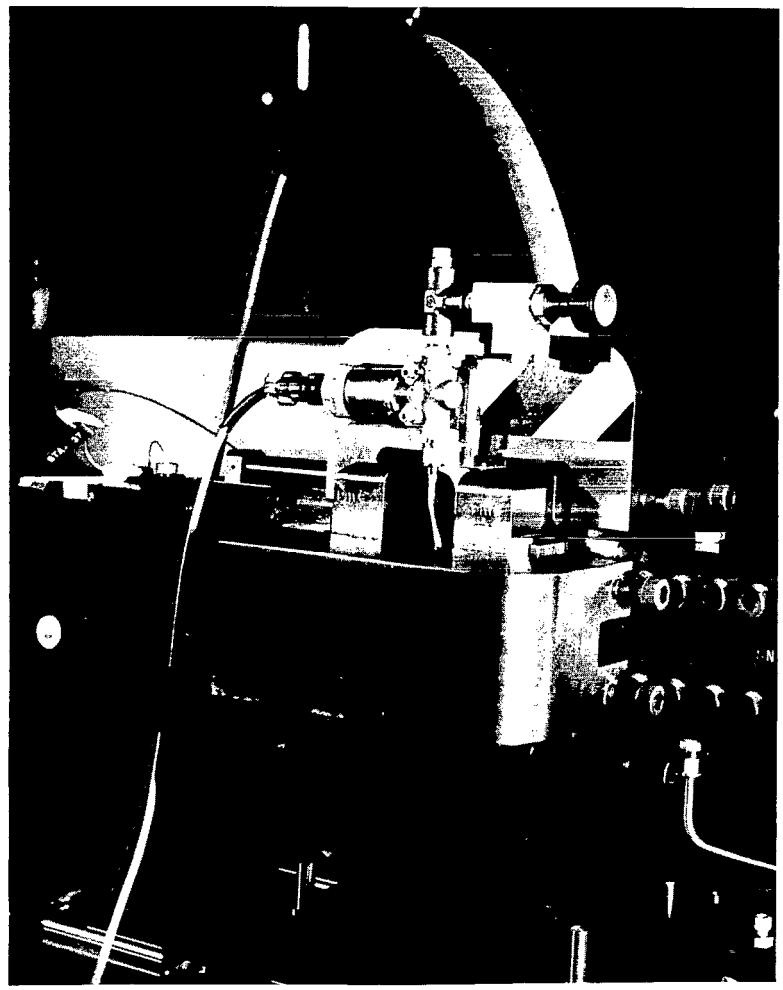

Figure 19—Secondary driver section showing vent valve and C-bar clamps.

that can be associated with the transmitted shock. The three solutions corresponding to these wave patterns are referred to as indicated earlier: (1) the auxiliary left-facing standing shock, (2) the auxiliary left-facing traveling shock, and (3) the auxiliary left-facing rarefaction wave. The experimental data required to validate the theoretical results, qualitatively and quantitatively, are presented and a comparison is made. Finally, an error analysis of the data systems used in the experimental program is detailed to enable a realistic assessment of the experimental verification of the theory.

Pressure ratios and wave speeds are the parameters used in the discussion of the results. These were selected primarily because they were major parameters computed in the theoretical portion of this work and correlation could be directly obtained from the experimental data. Parameters such as Mach number were computed from these primary measurements. Although temperatures were computed for the theoretical analysis, they are not presented in the discussion because temperature histories were not measured in the experimental program.

Theoretical Results

Two sets of theoretical computations for the primary model configuration (0.078-in.-diameter holes) were performed for the range of incident-wave Mach numbers previously discussed; one set was in accordance with the Rayleigh (or lower limit) duct-flow model and the second set was according to the Fanno (or upper limit) duct-flow model. In addition, a set of computations for incident-wave Mach number 3 was performed for the secondary model configuration (0.250-in.-diameter holes) in accordance with the Rayleigh model to examine the influence of a higher Reynolds number on the results. In all computations, the compatibility of the three possible types of auxiliary transmitted waves was examined.

The results of the analysis with the Rayleigh duct-flow model are presented in terms of computed quasi-steady pressure ratios in the flow regions upstream of the test model, at the model faces, and downstream of the model in Table 1.

For the range of incident-wave Mach numbers considered, 2 to 5, these computations did not indicate the validity of the left-facing auxiliary standing wave downstream of region 4. The solutions for the auxiliary standing-wave cases shown in the table may represent an interim state during the transient period of base-region pumping that could exist at a Mach number lower than that which must theoretically exist in region 4 to satisfy continuity and momentum. For these cases, at the conclusion of the initial base-region transient, the quasi-steady stable auxiliary solution would be more aptly represented by one of the second type (left-facing traveling wave) or one of the third type (left-facing rarefaction wave).

Table 1—Theoretical pressure ratios versus incident-wave Mach number for Rayleigh duct-flow model.

Model	Mach Number	$_2p_1$	$_3p_1$	$_Rp_1$	$_Ep_1$	$_Bp_1$	$_4p_1$	Solution	$_6p_1$
Primary (p_1 = 5 psia and T_1 = 535° R)	2	4.50	12.54	4.89	3.67	0.39	0.63	1	2.82
								2	3.05
								3	4.04
	3	10.33	40.19	13.72	10.27	1.13	1.77	1	4.25
								2	6.27
								3	8.20
	4	18.50	87.41	31.59	21.61	2.20	4.08	1	6.14
								2	11.43
								3	15.60
	5	29.00	150.60	54.70	42.70	4.56	7.62	1	9.62
								2	17.62
								3	21.40
Secondary (p_1 = 5 psia and T_1 = 535° R)	3	10.33	42.12	15.02	11.98	1.30	2.02	1	4.48
								2	6.74
								3	8.72

To arrive at these interim solutions of the first type, the conditions of state in region 4 were maintained and the Mach number was assumed to take on a lower value that would satisfy compatibility across the transmitted-wave contact surface. It should be noted that for an incident-wave Mach number of 2, the region 4 Mach number had to be lowered less than 7 percent from the value obtained from the impulse function (Equation 17) to enable this hypothetical compatibility; at an incident-wave Mach number of 5, the region 4 Mach number had to be lowered by 46 percent to produce similar agreement. In essence, at the low end of the Mach number range, the Rayleigh theory predicts the possibility of quasi-steady compatibility of the first type; but, as the strength of the incident wave increases, the theory definitely indicates that either the traveling wave or the rarefaction waves are the theoretically compatible auxiliary phenomena.

It should also be noted that the solution of the third type results in highest final pressure ratios, so that as incident-wave strengths are increased and the strength of the auxiliary wave decreases, the compatibility criteria, based on one-dimensionality of the quasi-steady fields, indicate that the appearance of a rarefaction wave (as predicted by Barthel (Reference 11)) is not likely since the pressure ratios predicted for this solution are significantly higher than that required for the left-facing auxiliary traveling shock wave. Since rarefaction waves are sound waves with relatively small pressure perturbations across their fronts, it is doubtful that this phenomenon would be evidenced as a simple auxiliary wave except at much higher incident-wave strengths than are being considered here.

The set of computations for the secondary test model demonstrated that the greater Reynolds number was no advantage as far as heat transfer was concerned. The higher Nusselt number was negated by larger hole diameter so that the net effective heat transfer coefficient was 14.5 percent lower, thus resulting in a lesser drop in stagnation temperature. This is reflected in the pressure ratios shown in Table 1. The duct exit-plane pressures are 16.66 percent higher for the model containing the 0.250-in. holes; transmitted pressure ratios for the three types of solutions are 5.4, 6.4, and 7.5 percent higher.

Table 2 indicates the velocities of the various waves as a function of the incident-wave Mach number. The final column of the table indicates that although the second solution wave speeds increase negatively, the particle velocities in region 4 increase at an even greater rate; thus the auxiliary waves (when referenced to a stationary coordinate system) appear to move downstream at a monotonically increasing rate.

The theoretical pressure ratios for the Fanno duct-flow model are shown in Table 3. They are, in general, significantly higher than those for the Rayleigh computations.

Theoretical wave speeds, shown in Table 4, in general, are slightly higher except in the case of second solution auxiliary-wave speeds. These are of comparable value for all incident-wave Mach numbers except 2. At this value, the second solution wave speed becomes zero or reverts to a standing wave. This is reinforced by the values of the primary transmitted-wave pressure ratios of the first and second solutions; their values are less than 1.4 percent apart. In addition, the solution of the first type indicates the full compatibility for a left-facing standing wave as an auxiliary solution in terms of all conditions of state and velocity at region 4.

Therefore, in accordance with the Fanno method of computation, at the initial incident-wave Mach number, the auxiliary transmitted wave (after the brief initial transient period) should be the

Table 2—Theoretical wave speeds versus incident-wave Mach number for Rayleigh duct-flow model (stationary coordinate system).

Model	Mach Number	Incident U_I (fps)	Reflected $U_R - u_2$ (fps)	Auxiliary-Wave Solution	Transmitted U_T (fps)	Auxiliary $U_A - u_4$ (fps)
Primary (p_1 = 5 psia and T_1 = 535° R)	2	2306	-943	1	1845	
				2	1916	90.7
				3	2190	
	3	3459	-1040	1	2242	
				2	2708	579
				3	3099	
	4	4612	-1171	1	2681	
				2	3663	1325
				3	4266	
	5	5765	-1368	1	3363	
				2	4535	1542
				3	5032	
Secondary (p_1 = 5 psia and T_1 = 535° R)	3	3459	-1042	1	2301	
				2	2802	619
				3	3102	

Table 3—Theoretical pressure ratios versus incident-wave Mach number for Fanno duct-flow model for the primary test model.

Mach Number	$_2p_1$	$_3p_1$	$_Rp_1$	$_Ep_1$	$_4p_1$	Solution	$_6p_1$
2	4.50	12.66	9.72	5.90	0.59	1	2.94
						2	2.90
						3	3.74
3	10.34	43.92	33.18	20.84	2.10	1	4.66
						2	7.16
						3	9.20
4	18.50	94.38	71.10	44.90	4.50	1	7.20
						2	12.86
						3	16.34
5	29.00	162.78	122.64	77.44	7.76	1	10.88
						2	20.74
						3	26.10

Table 4—Theoretical wave speeds versus incident-wave Mach number for Fanno duct-flow model for the primary test model (stationary coordinate system).

Mach Number	Incident U_I (fps)	Reflected $U_R - u_2$ (fps)	Auxiliary-Wave Solution	Transmitted U_T (fps)	Auxiliary $U_A - u_4$ (fps)
2	2306	-954	1	1882	
			2	1872	0
			3	2102	
3	3459	-1108	1	2345	
			2	2888	613
			3	3267	
4	4612	-1325	1	2897	
			2	3853	1105
			3	4337	
5	5765	-1569	1	3548	
			2	4881	1531
			3	5471	

left-facing standing wave; for higher values of the incident-wave strength, the auxiliary transmitted wave should be the left-facing traveling wave.

Hence, both the Rayleigh and Fanno theoretical flow models tend to predict similar auxiliary-wave patterns and parametric trends for the same incident-wave Mach number.

It should be noted that, in the Fanno limit series of computations, the area ratio used in Kochendorfer's method to compute the Mach number in region 4 was not the geometric ratio based on A_4/A_E, but instead, since the flow was assumed to choke at the exit plane, A_4/A^* was used. This is closer to a real case than the geometric area ratio since one would expect a significant thickness of the boundary layer at the exit plane. The progressive growth of the boundary layer along the length of the duct contributes to the choking of the duct and is the controlling factor in adjusting the mass flow and upstream stagnation conditions in region 3. A comparison of the stagnation zone pressure ratio ${}_3p_1$ in Tables 1 and 3 shows that the effect of the exit-plane choking is to provide (theoretically) up to 8-percent higher pressures upstream of the model than for the Rayleigh calculation of the duct flow.

To summarize the purely theoretical aspects of this work, the Rayleigh and Fanno calculations require similar auxiliary conditions for compatibility. The major difference between the two methods is that the Fanno duct-flow theory results in consistently higher pressure ratios throughout the entire range of up to 12.5 percent for all transmitted-wave solutions.

Theoretical computations were also performed for an ideal isentropic model assuming a vena contracta with supersonic duct flow and no vena contracta with sonic duct flow. The computed transmitted-wave strengths are plotted in Figure 26 and discussed in a later section.

Experimental Results

Qualitative Results

The high-speed photographs provided by the framing camera for the majority of the test runs verified the existence of the wave phenomena predicted by the theoretical computations. For both models, at the incident-wave strengths of 4 to 5.5, the primary transmitted wave was accompanied by an unstable auxiliary wave which oscillated during the initial transient at a position about 6 to 7 hole diameters downstream of the model and then assumed the fixed stable position of a standing wave about 8 to 9 hole diameters downstream of the model. For incident-wave strengths of 8.5 and higher, the primary transmitted wave was accompanied by a left-facing traveling shock as was predicted by the theoretical computations. In none of the test runs were any wave formations noted that could be interpreted as auxiliary rarefaction waves nor were there any pressure traces that showed the presence of rarefaction waves.

Both models, in general, exhibited the same basic wave formations in the upstream reflected-wave regions and in downstream transmitted-wave regions with one exception. In the case of the model with 0.078-in. holes, the primary transmitted wave rapidly developed as a plane wave and remained essentially a plane wave as it traveled downstream. The model that had the larger (0.250 in.) holes started as a curved wave with a parabolic bump at its center and very slowly flattened as it progressed down the tube. It did not lose its curvature completely while in the field of view and although the bump flattened, it was still evident at the edge of the optical field for the lower shock strengths. At higher incident-wave strengths, similar wave formations were noted with the appearance and disappearance of additional intermediate-wave formations between the primary wave and the auxiliary wave. The primary wave in traversing the length of the downstream window appeared to weaken and then strengthen and become a pair of plane traveling shocks, one located where the bump had been and one where the main curved front had been. The reason for the complexities associated with this model is a combination of effects that are present with the small hole model, but to a much lesser degree.

The 0.078-in.-hole model had at least 68.5 percent of its frontal area involved in its core flow; therefore, as far as the optical system was concerned, the zone of Coanda flow at the channel walls was quite small. Recompression shocks at the wall affected only the edges of the primary wave which appeared to fully dominate the net flow as it progressively developed. In the case of the model having 0.250-in.-diameter holes, only about 26.5 percent of the frontal area was involved in the central core flow, the remainder was associated with a Coanda flow at the channel boundaries. This permitted the core to progress more rapidly downstream producing the bump; the separated flow at the wall recompression produced the oblique shocks which then interacted with the core to provide the appearance of the curved wave and core bump. The intermediate waves that appeared and vanished as the primary wave traveled downstream could very readily have been caused by stagnation-region perturbations due to higher levels of turbulence in the field behind the reflected incident wave in the case of the larger holes.

It is apparent that 0.250 in. was not an optimum choice of hole size because of this higher turbulence level and the domination of the field by wall effects. In addition, since only 17 holes were involved as compared to 179 for the first model (to provide the same axial porosity), there was less

likelihood of developing a uniform front as rapidly as would occur with the many refracting waves that interacted in the model with small holes.

A model area scale factor of about 5 instead of the 10 used would have been preferable. This would have provided about 61 holes of 0.125-in. diameter to obtain the same porosity, but with much less turbulence and wall interference.

Figure 20 shows several frames of the framing camera record from run 22. The incident-wave strength was 17.73 and the sequence shown is for that portion of the cycle after the incident wave reflected from the upstream face of the model. The reflected wave appeared to start out as a plane wave and rapidly bent at the edges when interacting with the boundary layer produced by the incident wave. A very turbulent field was produced behind the reflected wave. Downstream of the model, the primary transmitted wave was generated as a plane wave except at the region near the walls. The wall interaction produced the appearance of a thick blurred wave. It was rapidly followed by an auxiliary wave that was initially curved because of wall effects, but rapidly became plane at its central core

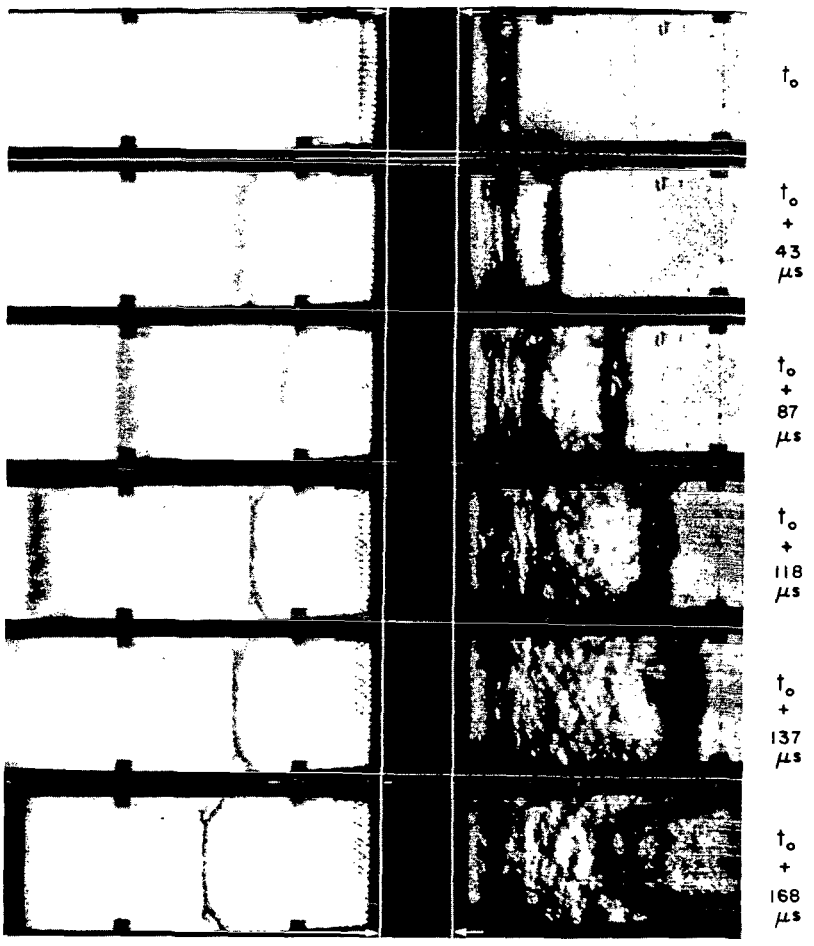

Figure 20—Framing camera record for run 22 taken at 160 750 frames per second with incident-wave strength $S_I = 17.73$; arrows indicate true locations of model faces.

with classic lambda shocks produced by interaction with the boundary layer generated by the primary transmitted wave. Careful examination of the auxiliary wave indicated that the increased turbulence levels in the reservoir zone produced a progressive asymmetry of the wave.

The increased turbulence was also evident in the oscillographs that were taken of the outputs of the pressure transducers located upstream and downstream of the model. Figure 21 shows the oscillograph records for run 5, which had an incident-wave shock strength of 5.27. The reflected-wave pressure oscillations were about twice that of the incident wave. The reflected wave had the typical abrupt increase in pressure initially, but then because of flow through the wall perforations and the blending of rarefactions from the holes and shocks from the solid portions of the wall, the pressure discontinuity became less abrupt as illustrated in Figure 21a. The downstream transmitted pressure waves appeared to have minimal turbulence. The records shown in Figure 22 were taken for run 22 at an incident-wave shock strength of 17.73. Increased turbulence levels were noted for the reflected waves. The pressure oscillations were of the order of five times those of the incident waves and the transmitted pressure waves were now very turbulent with the evidence of reinforcement by reflections. The reflected-wave heating effect on upstream transducer output was also apparent when the normal leveling of the pressure in trace was followed by a subsequent output increase at a lower rate.

Figure 23 shows the similarity of traces for the large-hole model at an incident-wave shock strength of 21.86. The upstream turbulence was slightly higher than shown for the small-hole model in Figure 22, but the downstream turbulence was about doubled. In both cases the records became more difficult to analyze because of heating and pressure perturbations caused by the turbulence.

Quantitative Results

Tables 5 and 6 indicate the measured incident-wave speeds and incident-wave strengths for the primary and secondary models, respectively.

Incident-wave speeds were measured over a 2-in. interval (2 in. from the model) from the oscilloscope time-pressure histories and also over two 10-in. intervals upstream of the model by electronic counters. Plots of the three measurements as a function of position indicated that wave-speed attenuation measured by counter readings was random and, in general, negligible. The measurements taken from oscilloscope records provided the appearance of greater attenuation rates of incident speed than the counter measurements, but these differences were of the same order of magnitude as the probable error predicted by error analysis. Measurements from film records (e.g., Figure 20) were not usable for reasons discussed in the later section on error analysis.

Therefore, the means of the counter readings were used to establish the shock-tube calibration curve shown in Figure 24. In general, most of the data points are within a ±5 percent error band. A small percentage of the plotted points exceed this limit, but are still within a 10 percent band.

This is not unusual with this type of apparatus because, as has been indicated by Winkler,[1] variations from ideal theory will occur because of variations in wave formation caused by anomalous diaphragm rupture, and partial mixing of the helium driver gas with the nitrogen driven gas. The

[1] E. Winkler, Naval Ordnance Laboratory, June 23, 1971.

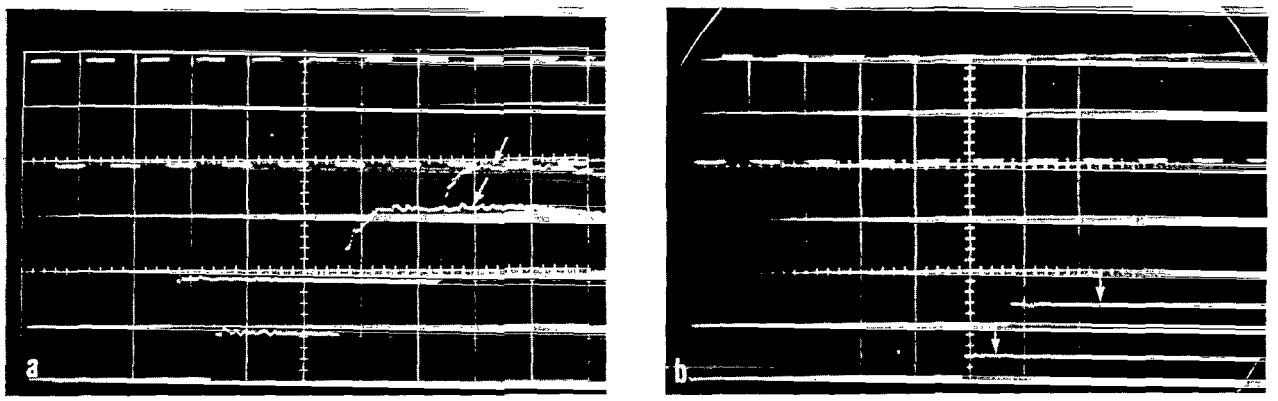

Figure 21—Oscilloscope records for run 5; incident-wave strength S_I = 5.27 with primary model; calibration frequency = 10.071 kHz. (a) Upstream pressure traces taken at stations 118 and 120; calibration amplitude = 0.051 V/cm. (b) Downstream pressure traces taken at stations 2D and 4D; calibration amplitude = 0.050 V/cm.

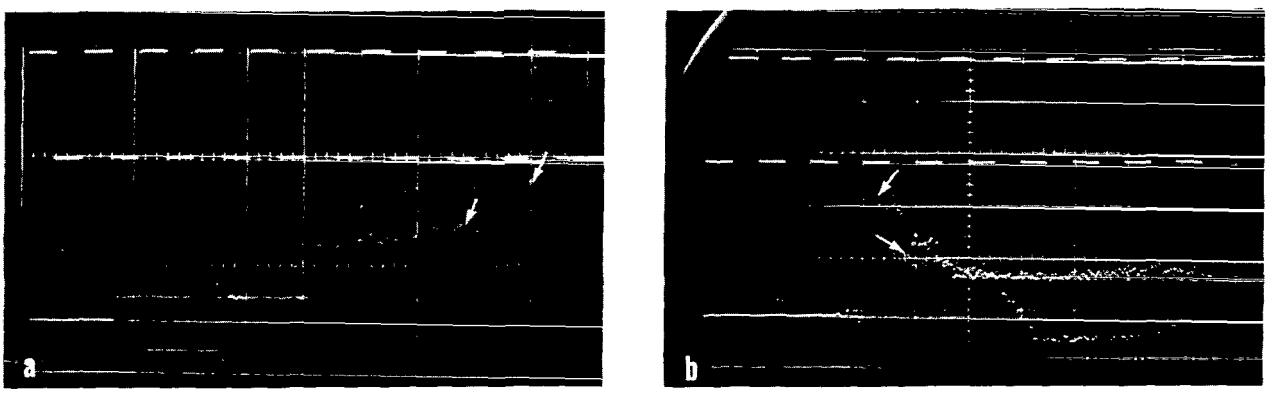

Figure 22—Oscilloscope records for run 22; incident-wave strength S_I = 17.73 with primary model; calibration frequency = 9.955 kHz. (a) Upstream pressure traces taken at stations 118 and 120; calibration amplitude = 0.495 V/cm. (b) Downstream pressure traces taken at stations 2D and 4D; calibration amplitude = 0.049 V/cm.

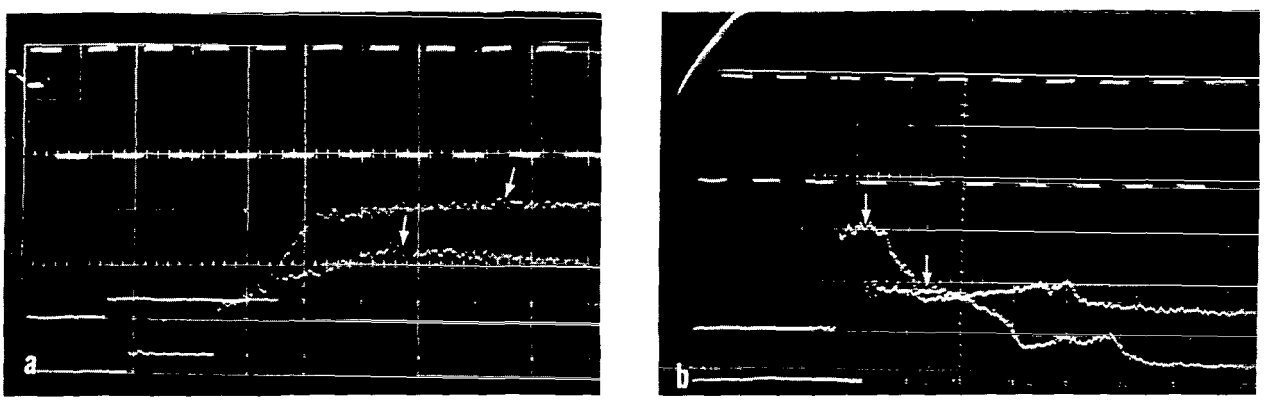

Figure 23—Oscilloscope records for run 40; incident-wave strength S_I = 21.86 with secondary model; calibration frequency = 10.975 kHz. (a) Upstream pressure traces taken at stations 118 and 120; calibration amplitude = 0.502 V/cm. (b) Downstream pressure traces taken at stations 2D and 4D; calibration amplitude = 0.049 V/cm.

Table 5—Experimental values of incident-wave speeds and shock strengths for the primary model.

Run No.	Cathode-Ray Oscilloscope, Stations 118 and 120			Counters, Stations 100 and 110		Counters, Stations 110 and 120	
	$_2p_1$	M_I	U_I (fps)	M_I	U_I (fps)	M_I	U_I (fps)
1	4.23	1.940	2237	–	–	2.030	2340
2	5.35	2.025	2334	–	–	2.220	2553
3	–	–	–	2.198	2534	2.213	2552
4	5.31	2.098	2419	2.228	2568	2.236	2578
5	5.27	2.120	2441	2.220	2561	2.240	2581
6	5.53	2.062	2378	2.239	2581	2.244	2587
7	9.64	2.810	3240	2.990	3448	2.995	3454
8	9.73	2.809	3239	2.994	3452	2.879	3320
9	9.37	2.664	3072	2.930	3379	2.929	3378
10	8.50	2.668	3076	2.785	3211	2.809	3238
11	9.66	2.895	3338	3.010	3469	3.030	3496
12	11.91	2.920	3367	3.224	3717	3.270	3771
13	12.14	3.170	3660	3.234	3729	3.266	3766
14	10.71	3.085	3558	3.077	3548	3.091	3564
15	12.20	3.083	3555	3.257	3756	3.291	3795
16	11.96	3.176	3661	3.259	3757	3.294	3798
17	17.80	3.567	4113	3.969	4577	3.965	4571
18	17.78	3.911	4509	4.155	4791	4.118	4748
19	–	–	–	4.337	5000	4.054	4674
20	17.08	3.758	4332	4.079	4704	3.809	4393
21	17.75	3.896	4492	4.131	4763	3.816	4400
22	17.73	3.631	4187	4.041	4660	4.031	4627
23	21.80	4.423	5100	4.602	5306	4.531	5225
24	20.99	4.156	4792	4.553	5249	4.478	5163

greatest dispersion from ideal theory (not attributable to probable error) occurs at Mach numbers above 4. However, these are within the range reported by experimenters in well-established facilities (Reference 32).

The data for runs where excessive leaks were known to exist were not included in Figure 24 as indicated in the later discussion of rest-region pressure errors.

Values of reflected- and transmitted-wave strengths are tabulated as functions of the incident-wave strength in Tables 7 and 8 for the small-hole and large-hole models. All values represent the mean of

Table 6—Experimental values of incident-wave speeds and shock strengths for the secondary model.

Run No.	Cathode-Ray Oscilloscope, Stations 118 and 120			Counters, Stations 100 and 110		Counters, Stations 110 and 120	
	$_2p_1$	M_I	U_I (fps)	M_I	U_I (fps)	M_I	U_I (fps)
25	5.29	2.063	2378	2.209	2548	2.223	2563
26	5.16	2.065	2381	2.192	2527	2.196	2531
27	5.44	2.200	2537	2.217	2556	2.254	2599
28	5.07	2.109	2432	2.161	2492	2.217	2556
29	5.13	2.021	2330	2.191	2526	2.203	2540
30	9.61	2.735	3154	2.952	3404	2.984	3441
31	9.86	2.663	3071	2.895	3338	2.923	3370
32	9.57	2.659	3065	2.921	3368	2.938	3388
33	8.74	2.797	3227	2.869	3307	2.875	3315
34	9.23	2.589	2986	2.801	3230	2.805	3234
35	12.72	2.815	3245	2.962	3415	2.995	3454
36	1.215	3.076	3547	3.072	3542	3.107	3583
37	13.07	2.889	3331	3.042	3508	3.098	3572
38	13.52	2.895	3337	3.038	3503	3.083	3555
39	13.13	2.980	3438	3.116	3593	3.119	3600
40	21.86	3.612	4165	3.591	4140	3.747	4320
41	20.09	3.760	4336	3.852	4442	3.820	4405
42	21.50	3.500	4037	3.690	4255	3.688	4252
43	22.88	3.500	4036	3.888	4483	3.676	4239
44	—	—	—	3.709	4277	3.705	4271
45	19.48	3.758	4332	3.824	4409	3.800	4381
46	12.39	2.747	3167	2.836	3270	2.855	3291

the peak values of two data traces exclusive of reducible heating effects. (Effects of pressure gage heating are discussed in a later section.)

The reflected-wave strengths were plotted against incident-wave strengths for the two test models in Figure 25. Also plotted, for purposes of comparison, were the curves for the ideal solid-wall reflected-wave strengths and those values predicted by the Rayleigh and Fanno duct-flow theories.

Since the curves for the theoretical data were less than 10 percent apart, the error bands shown are for +10 percent for the upper-limit solution and -10 percent for the lower-limit solution. For values of incident-wave strength below 15, the experimental data indicate that the simpler Fanno theory very closely predicts reflected wave strengths with an accuracy of better

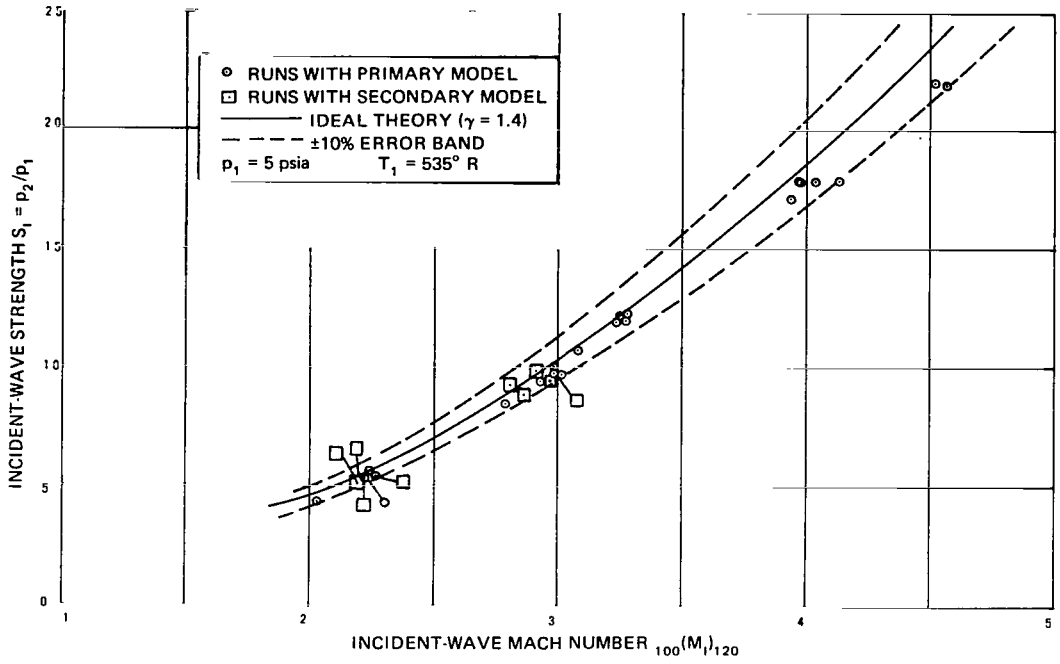

Figure 24—Shock-tube calibration based on counter measurements of wave speeds.

Table 7—Experimental values of mean peak reflected- and transmitted-wave strengths for the primary model.

Run No.	$_2p_1$	$_3p_1$	$_6p_1$	Run No.	$_2p_1$	$_3p_1$	$_6p_1$
1	4.23	11.77	2.35	13	12.14	52.86	7.49
2	5.35	16.26	2.88	14	10.71	52.00	6.59
3	—	—	—	15	12.20	54.12	7.33
4	5.31	16.91	2.66	16	11.96	53.92	7.39
5	5.27	16.19	2.97	17	17.08	74.04	9.77
6	5.53	17.31	3.11	18	17.78	101.98	10.53
7	9.64	39.57	5.66	19	—	—	—
8	9.73	39.91	5.73	20	17.08	96.80	10.62
9	9.37	37.94	5.42	21	17.75	90.33	8.91
10	8.50	34.33	5.01	22	17.73	87.98	10.05
11	9.66	38.37	5.26	23	21.80	115.74	12.75
12	11.91	55.27	7.41	24	20.99	126.10	11.92

Note: p_2 and p_3 measured at stations 118 and 120; p_6 measured at stations 2D and 4D.

Table 8—Experimental values of mean peak reflected- and transmitted-wave strengths for the secondary model.

Run No.	$_2p_1$	$_3p_1$	$_6p_1$	Run No.	$_2p_1$	$_3p_1$	$_6p_1$
25	5.29	16.23	3.15	36	12.15	55.14	7.71
26	5.16	14.34	3.05	37	13.07	58.70	8.13
27	5.44	16.48	3.12	38	13.52	57.90	8.20
28	5.07	15.52	2.91	39	13.13	56.81	7.93
29	5.13	15.81	2.92	40	21.86	110.17	11.67
30	9.61	36.73	5.26	41	20.09	102.11	11.96
31	9.86	39.23	5.62	42	21.50	106.35	12.85
32	9.57	38.81	5.48	43	22.88	108.54	13.27
33	8.74	35.96	5.50	44	—	—	13.34
34	9.23	37.25	5.67	45	19.48	97.65	13.45
35	12.72	55.90	7.81	46	12.39	55.83	8.11

Note: p_2 and p_3 measured at stations 118 and 120; p_6 measured at stations 2D and 4D.

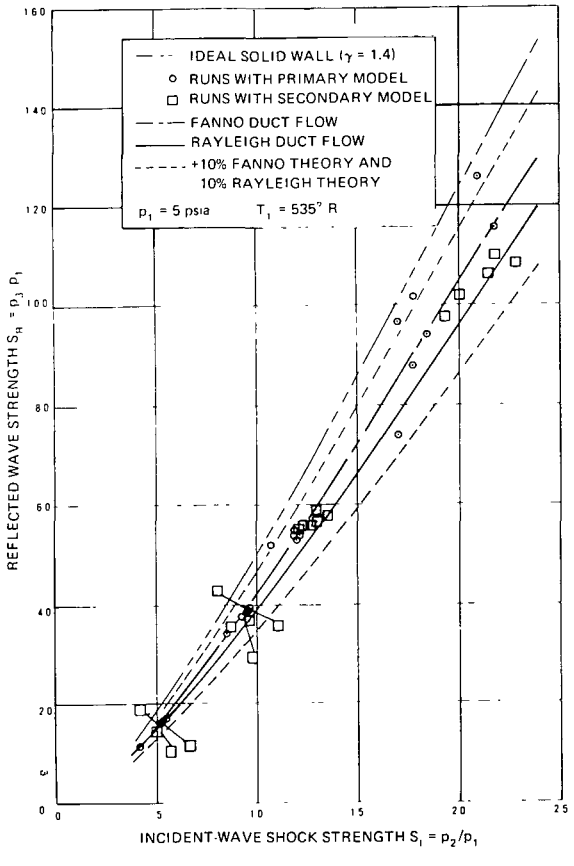

Figure 25—Reflected-wave strengths as a function of incident-wave strengths.

than 5 percent. However, at values above an incident-wave strength of 15, the dispersion became significantly wide with several of the data points exceeding the +10 percent Fanno limit. This can be the result of the greater possibility of anomalous diaphragm rupture with the thicker diaphragm units required to produce the higher values of incident shock strength, the resultant mixing of driver and driven gas, and the region of very complex mixing of shock and expansion waves at the upstream face of the model by these gas mixtures. These complexities were indicated for very weak shock waves by Rudinger (Reference 13) for a single-hole pattern where incident pressure ratios of 1.0 to 2.4 were being considered. For the stronger waves and the multiplicity of perforations of concern here, it is reasonable to expect a wide range of deviations to be experienced. However, at no time did any of the data points fall outside the ideal solid-wall curve so that the ideal absolute limit on test data dispersion was not exceeded.

The experimental values of reflected- and transmitted-wave speeds were tabulated for the small-hole and large-hole models in Tables 9 and 10, respectively, for the full range of incident-wave shock strengths. Although similar considerations concerning wave attenuation and correlation of measurements by oscilloscope and counter techniques apply here as for the incident-wave speed measurements, the close correlation of the reflected-wave speeds should be noted. This is not unusual when one considers that the reflected wave is slow moving and therefore can be more accurately measured from the oscilloscope record than either the incident or transmitted waves. Therefore, dispersion of values can be minimal. This is also seen to be the case for the lower values of the transmitted wave speeds. When incident shock strengths increase above a value of 10, the spread between oscilloscope and counter wave speeds also increases.

It is interesting to note that the values of wave speeds shown in Tables 9 and 10 when compared with the values predicted by the Rayleigh and Fanno theories (Tables 2 and 4, respectively) indicate good correlation in terms of the predicted and experimental auxiliary-wave solutions as a function of the incident-wave shock strengths.

Comparison of Theoretical and Experimental Results

The average of the peak values of transmitted-wave pressure ratios as computed from measurements (at arrows in Figures 21 to 23) of the dual downstream transducer outputs were plotted as a function of the incident-wave strengths in Figure 26a. The theoretical curves for the auxiliary standing- and traveling-wave solutions of the Rayleigh and Fanno duct-flow models were plotted on the same graph.

As predicted by theory and demonstrated physically by means of the high-speed photographic records, the data points for an incident-wave strength of about 5 fall within the predicted curves for the auxiliary standing wave. The data points for higher values of incident-wave strength coincide with the curves for the auxiliary left-facing traveling-wave solution. Figure 26b is an enlargement of the initial section of Figure 26a. It shows the major portion of the data points for both auxiliary solutions lie on the Rayleigh duct-flow curves. The theoretical curves are very close to each other for the same auxiliary-wave solution. The difference between theories for each solution is about 15 percent. The correlation of the experimental data with the Rayleigh solution, in general, is better than 5 percent in the range of incident-wave strengths below 15 and the same order of correlation is

Table 9—Experimental values of reflected- and transmitted-wave speeds for the primary model.

Run No.	$_2p_1$	$U_R - u_2$ (fps)		U_T (fps)		
		Cathode-Ray Oscilloscope, Stations 118, 120	Counter, Stations 118, 120	Cathode-Ray Oscilloscope, Stations 2D, 4D	Counter, Stations 4D, 12D	Counter, Stations 12D, 22D
1	4.23	-929	–	1845	–	1801
2	5.35	-1005	-1008	2032	1953	1972
3	–	–	-1018	–	1938	1982
4	5.31	-941	-952	2300	2568	2577
5	5.27	-933	-955	1947	[a]1976	[a]1976
6	5.53	-925	-940	1930	1969	2025
7	9.64	-1051	–	2650	2612	2640
8	9.73	-1080	–	2325	2616	2644
9	9.37	-1062	–	2581	2560	2585
10	8.50	-1044	–	2396	2444	2473
11	9.66	-1102	–	2623	2631	2658
12	11.91	-1203	–	2907	2907	2946
13	12.41	-1171	-1169	2693	2899	2934
14	10.71	-1087	-1070	2508	2757	2793
15	12.20	-1117	-1132	2911	2925	2957
16	11.96	-1196	-1189	2562	2925	2952
17	17.80	-1413	-1417	3224	3440	3474
18	17.78	-1447	-1465	3487	3592	3631
19	–	–	-1432	–	–	–
20	17.08	-1409	-1385	3470	[a]3605	[a]3605
21	17.75	-1424	-1394	3472	3552	3623
22	17.73	-1413	-1422	3351	3480	3544
23	21.8	-1552	-1572	3707	[a]3921	[a]3921
24	20.99	-1559	-1545	3670	3872	3913

[a]These values are computed from readings at stations 4D and 22D.

evident at higher shock strengths with a few isolated points just outside the ±10 percent error band of the Rayleigh theoretical curves. Those values outside the error band were dispersed equally about the theoretical curve and can be attributed to the greater influence of leakage on the computation of transmitted-wave strengths and the influence of the complex transient processes as a result of the more turbulent mixing of shock and expansion waves during downstream transients. Since the data points involved were those obtained with the secondary model (0.250-in.-diameter holes), this greater deviation can also be attributed to the very complex three-dimensional fields produced by a combination of the normal downstream transient fields coupled with the significant Coanda effect of the wall interactions. These very turbulent and complicated flows can very readily deviate from the simple one-dimensional theories utilized because of greater variations in entropy and localized shock phenomena.

Error Analysis of Experimental Data Systems

Pressure Instrumentation

Each of the components of the pressure data system affects the accuracy of the acquired time-pressure histories. To realistically assess overall reduced data limitations, the transducer and its

Table 10—Experimental values of reflected- and transmitted-wave speeds for the secondary model.

Run No.	$_2p_1$	$U_R - u_2$ (fps)		U_T (fps)		
		Cathode-Ray Oscilloscope, Stations 118, 120	Counter, Stations 118, 120	Cathode-Ray Oscilloscope, Stations 2D, 4D	Counter, Stations 4D, 12D	Counter, Stations 12D, 22D
25	5.29	-925	–	2074	–	–
26	5.16	-949	-953	2032	1998	1979
27	5.44	-912	-983	2136	2043	2035
28	5.07	-919	-925	1959	1974	2025
29	5.13	-925	-929	2037	2011	2006
30	9.61	-1024	–	2711	2619	2623
31	9.86	-1006	–	2914	2572	2571
32	9.57	-1069	–	2638	2591	2600
33	8.74	-1028	–	2648	2544	2553
34	9.23	-1059	–	2524	2486	2491
35	12.72	-1053	-1062	2682	[a]2717	[a]2717
36	12.15	-1148	–	2814	2776	2835
37	13.07	-1070	-1072	2747	2774	2910
38	13.52	-1092	-1087	2749	2773	2823
39	13.13	-1135	-1137	2750	2770	2813
40	21.86	-1090	-1097	3796	4201	4861
41	20.09	-1330	-1331	3436	3389	3418
42	21.50	-1286	-1301	3148	[a]3688	[a]3688
43	22.88	-1272	–	3060	3335	3556
44	–	–	-1411	–	3381	3511
45	19.48	-1376	-1459	3082	3389	3443
46	12.39	-1010	-1133	2304	2473	2670

[a]These values are computed from readings at stations 4D and 22D.

auxiliary electronics, the recording instrumentation, the calibration trace instrumentation, and data reduction methods must be considered in terms of their influence on pressure amplitude and time base errors. This is especially important since wave speeds deduced from pressure traces should correlate with those measured directly by electronic counters.

The amplitude errors due to combined calibration errors of standards, transducer, and charge amplifier are no greater than 1.2 percent of data point value. The error due to calibration trace amplitude instability can be as high as 4 percent at 50 mV to 1 percent at 500 mV. The data reduction errors based on a 0.005-in. trace resolution produces an additional error of 5 percent for traces of 0.10-in. length to 1 percent for traces of 0.500-in. length. This means that for low-level pressure signals, it is conceivable that cumulative pressure magnitude errors of 10 percent maximum are possible. This error is reduced for the higher values of pressure to approximately 3.5 percent for reduced data.

Since the pressure traces were also used to obtain incident- , reflected- , and transmitted-wave speeds, the stability and linearity of the oscilloscope sweep rate, the calibration trace frequency, and the trace reading error become significant factors. The oscilloscope manufacturer's data (References 33 and 34) indicate a maximum full-scale sweep error of 3 percent at any point along the central 8 cm of the 10-cm graticule. At the frequencies set for the pulse generator that provides the calibration

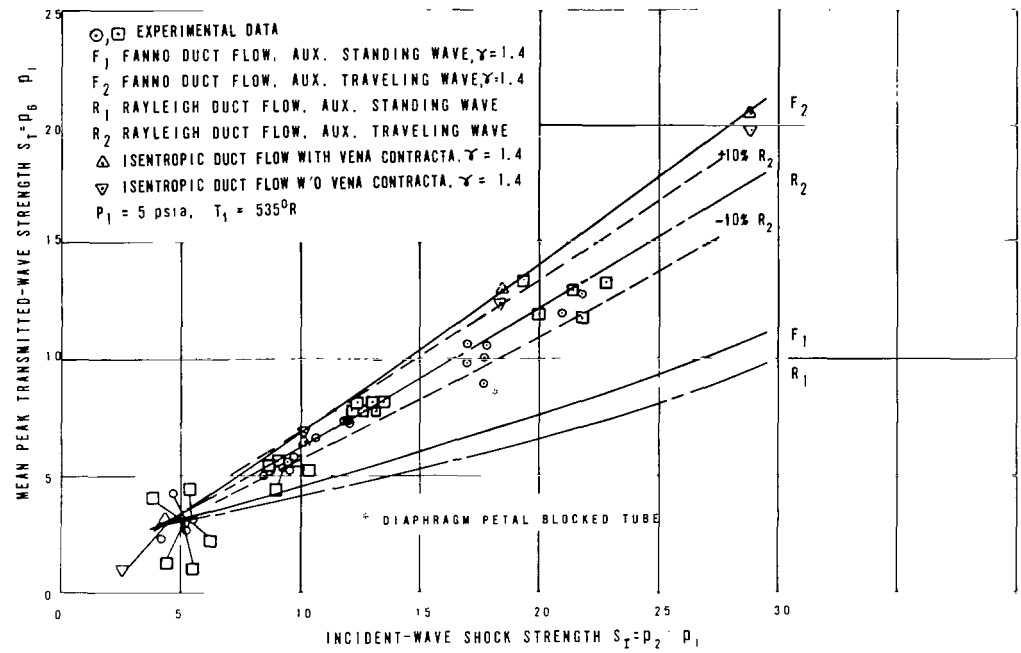

(a)

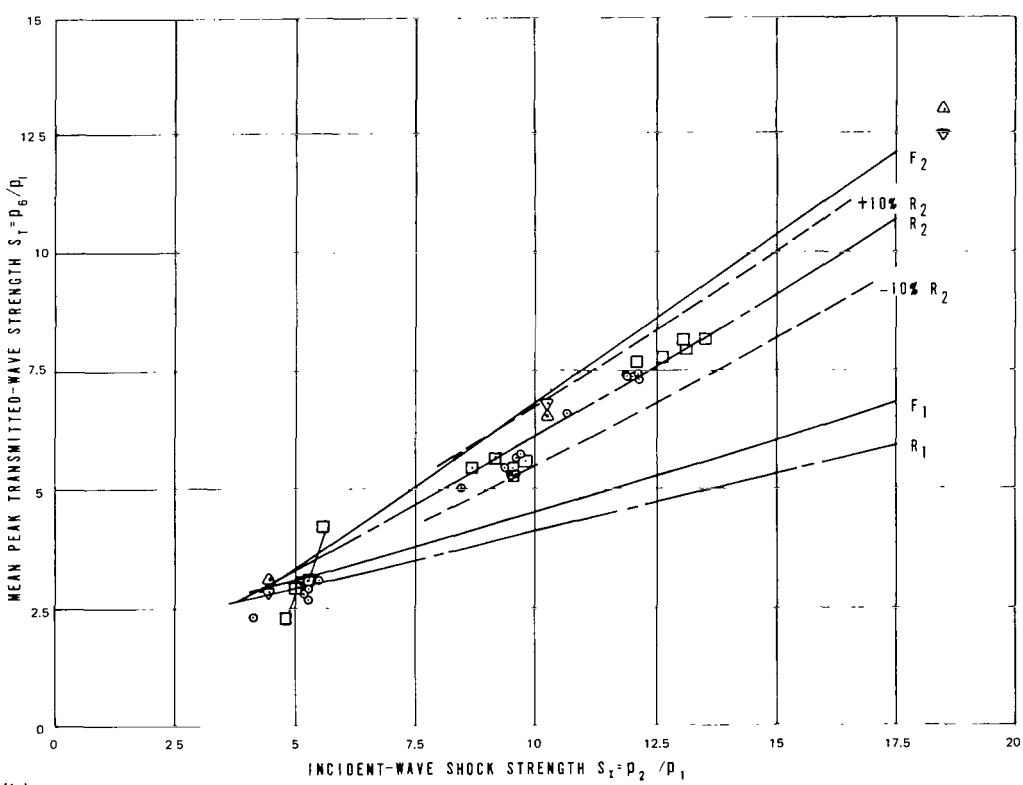

(b)

Figure 26—Primary transmitted-wave strength as a function of incident-wave strength. (a) Complete graph. (b) Initial portion of graph, expanded for clarity.

square wave, a ½ percent rate instability was recorded during the test program. Therefore, equipment errors alone can provide a maximum error of 3½ percent. The trace reading error for low-velocity waves (such as reflected waves) results in reduction errors of about 1 percent; however, for fast-moving waves where the trace length between points of interest are on the order of 0.100 in., the reduction error can increase to a maximum of 5 percent. Therefore, if the pressure traces are used to establish local wave speeds, the possible error range can be from 4½ to 8½ percent of the true value.

The final factor that must be considered is the effect of transducer heating errors due to the high stagnation temperatures occurring behind the reflected incident shock at the upper end of the incident-wave test range.

Temperatures on the upstream side of the model can increase by 3000 F° over the initial ambient of 535° R. Since the transducer manufacturer claims a 0.01 percent output for every Fahrenheit-degree temperature rise, if the transducer assumed the gas temperature, it could conceivably have an error of +30 percent. However, the gas medium is transparent to radiation in the temperature range expected, and the testing time is too short for the transducer to establish these temperatures through conduction and convection heat transfer.

Discussions of this problem with personnel of the Naval Ordnance Laboratory[2] indicated that they have considered this problem on a limited basis. Aronson of the Aeroballistics Division has attempted to insulate such transducers by means of 6-mil black electrical tape. He has measured amplitude differences of 3 to 5 percent for incident-wave Mach numbers of 5 to 8 by this method. The effect of additional thicknesses on reducing thermal error were not considered because of a falloff in dynamic response with the 6-mil tape. This technique was established on a trial and error basis because of the complexity of an analytical approach to the heat transfer involved. Therefore, there is no way to establish the absolute effectiveness of this technique. McLain (Reference 35) has also noted piezo-electric transducer baseline shift during combustion stability studies of N_2H_4/N_2O_4 reactors. He attributed this shift to radiation from the combustion products and assessed the amplitude of the shift by a composite time-pressure history lasting 5 ms with a 100 μs/cm sweep rate.

The effect of heating was taken into account in the current investigation by careful examination of the pressure trace. Unlike McLain's situation, the time-pressure traces were relatively clean and it was possible to visually determine where the maximum output occurred prior to heating by the leveling off of the trace and then by the abrupt increase in slope with additional amplitude growth as heating occurred. This effect is sufficiently distinctive so that it is not obscured by the high turbulence levels occurring after reflection from the perforated wall of the model. In Figure 22a, this effect is plainly evident in the upper trace of the reflected wave. The peak indication is marked by a white arrow; however, this includes the heating effect and is followed by the cooldown portion of the trace. Exactly 3 cm to the left of the white arrow (vertical lines on graticule are 1 cm apart) is the place where peak pressure was actually measured. It is seen that at this location in time there is a zero slope to the mean pressure indicating that the trace had hit the limit of its initial rapid rise. Further increase in amplitude was attributed to the slower rate occasioned by heat transfer. The lower trace on this same photo reaches its peak pressure 2 cm to the left of its corresponding white arrow. All traces produced by incident-wave strengths above 15 were reduced in this manner. The traces at lower

[2]E. Winkler, A. Seigel, and P. Aronson, June 23, 1971.

values of wave strength were not sufficiently distinctive to employ this visual technique, and therefore temperature was not considered to be of consequence in contributing to data reduction errors.

Rest-Region Pressure Errors

To very accurately reproduce initial conditions, a master vacuum gage having 1.0-mm-Hg divisions was used to charge the driven section to 501.5 mm Hg with nitrogen. Unfortunately, the gage had to be valved off prior to firing the shock tube to prevent damage to it by reflected shocks transmitted in the lines. Therefore, for every run there was a period of about 2 min before a firing in which the rest-region pressure was not being monitored with precision equipment.

During the testing of the secondary model, leaks developed in the driven section after run 34 so that it was not possible to pump down on the scavenging part of the test cycle to the required 0.5 mm Hg. Attempts were made to compensate for the leak by a vacuum bleed during test countdown. Examination of the data for runs 35 through 46 showed that shock strengths computed on the basis of the rest-region pressure being $p_1 = 5$ psia resulted in incident wave-speed values considerably lower than predicted by ideal theory. On the basis of ideal theory, it was computed that the rest-region pressures ranged from an average value of 6.01 for runs 35 to 39 to 6.66 for runs 40 to 46. Apparently the leak had grown progressively worse with further testing. To avoid complete loss of the data, those presentations that involved the pressure ratio in only one of the variables excluded the questionable data points; those presentations for which the error was compensated by having the rest-region pressure common to the dependent and independent ordinate retained all data for purposes of data analysis.

Wave-Speed Instrumentation Errors

Although the electronic counter system accuracy depends primarily on the precise adjustment of its crystal clock in accordance with the U.S. Bureau of Standards worldwide radio time signal (WWV) standards, the auxiliary circuitry used for the amplification and the gating of timing signals could introduce considerable error. Since differences between individual readings were utilized, the zero errors for common stop signals were of importance. These produced no difficulty on forward traveling waves; but on reflected-wave circuits, zero errors ranging from 5 to -10 μs were noted. These errors were a function of wave strength, wave shape, and the aging characteristics of the equipment. For incident-wave strengths in the range of 9 to 10, it was not possible to obtain reliable triggering of the pulse-counting gate so that reflected-wave speeds were not obtained directly by counter measurement. On other runs, where required, correction factors to compensate for zero error were included.

Optical System Errors

The optical instrumentation, although adequate for qualitative studies, provided data of questionable validity when considered quantitatively. There seemed to be excessive, random deviations from the mean of wave velocities measured from the framing camera film strips. The measuring errors at low velocities were quite high since the frame-to-frame wave movement was on the order of 3 to 10 times the smallest measurable increment of 0.010 in. Thus errors on the order of 10 to 30 percent were possible if the optical components were perfect and introduced no additional inaccuracies. At

higher wave speeds, the error was on the order of 5 to 10 percent; the maximum and minimum deviations from the mean were significantly less for these runs, but still not comparable to data obtained from counter or oscilloscope records.

This was evident when velocity-time measurements obtained from the film frames were plotted. Very random oscillatory values for wave speed were obtained. The oscillations were of a significantly high percentage of the velocity amplitude. In addition to the errors in resolution were the distortion errors resulting from the plastic windows that were substituted for damaged optical flats. They were out of flat and parallel by as much as 0.005 to 0.010 in. and had considerable waviness and local discontinuities (such as rounded edges, pits, fine scratches) that served to obscure weak wave fronts and produced interference bands at model/window interfaces.

The camera optics also contributed to deviations from an ideal system in the space dimension. Time resolution was more than adequate since mirror turbine speeds were continuously monitored by an electronic counter built into the camera control console. The major error sources were the precision of the alignment of the individual relay lens and mirror systems (80 of them) and the variable length of the optical lever arm from frame to frame. It is not possible to attach numbers to these errors since the alignment was accomplished visually on each system. A rigorous study of the vibration modes of the 80 mirror mounts, the relay lens systems, and the input optics would probably indicate the possibility of deviations due to mechanical and aerodynamic excitation of elastic elements of the component structures and possible magnification of these vibrations due to transmissibility of the camera housing and base supports.

Because of the large number of intangibles that did not permit an adequate quantitative error analysis, the wave speeds measured from the camera data were not presented. However, except in the immediate vicinity of the model (about 1/8-in. upstream and downstream), the high-speed record helped resolve and verify the adequacy of the assumption of one dimensionality of the wave fronts, the verification of auxiliary transmitted-wave solutions, and extent of wall effect on channel flows.

Test Medium Variability Effects

The test fluid was dry nitrogen with a dewpoint of - 105° F; for all practical purposes the presence of trace quantities of water vapor was negligible. However, during runs 35 through 46, ambient air leaked into the rest region. Since the ambient atmosphere had a 50 percent relative humidity, computations were performed to examine the effect of air and water vapor contamination on the nitrogen charge of the driven section. The effect on γ was negligible; for final rest-region pressures of 6 and 6.5 psia in the driven section, the gas constant was reduced by 0.24 and 0.34 percent, respectively. Since the major influence of the gas constant is reflected in the computation of the sound speed, which is a function of the square root of the gas constant, the error contributed by gas constant change can also be neglected.

CONCLUSIONS

Limitations of Theoretical Work

The theory as outlined herein predicted the reflected-incident-wave strengths to within a 5 percent accuracy for incident-wave strengths of 4 to 15; for incident-wave strengths between 15 and 25, the

reflected-wave strengths were within 10 percent accuracy. These values are valid when the Fanno duct-flow model is employed.

When using the Rayleigh model for predicting reflected-wave strengths, the predicted values were on the low side by slightly over 5 percent for the full range of incident shock strength.

The Rayleigh theory verified the nature of the transmitted auxiliary waves for the full range of the incident shock strengths considered. It also predicted transmitted-wave shock strengths with an accuracy better than 5 percent in the range of incident-wave strengths of 4.5 to 15, and predicted transmitted-wave shock strengths with an accuracy of ±5 to +10 percent in the incident-wave strength range of 15 to 25.

The Fanno theory predicted the nature of the transmitted auxiliary waves more accurately than the Rayleigh theory; but this simpler approach enabled the prediction of transmitted-wave strengths to no better than 10 to 15 percent over the entire range of incident-wave shock strengths.

Examination of the data in Figure 26 indicates that the transmitted-wave shock strengths were 60 percent of the incident-wave strengths throughout the test range. Transmitted-wave speeds averaged about 77.5 percent of incident-wave speeds.

Limitations of Experimental Work

The experimental program was hampered by a less than optimum optical system. The use of plastic windows degraded optical performance to the degree that quantitative data were not reliable. The defects (previously outlined) also served to obscure details of the flow in close proximity to the model surfaces. However, these same windows were adequate for the purpose of qualitatively defining physical details of wave formulation, boundary-layer interaction, and wall effects.

Piezoelectric transducers performed satisfactorily in providing time-pressure histories with rest-region conditions as the zero ground level. In perfectly sealed systems, a precision vacuum gage reading of rest-region conditions provided data of desirable accuracy. However, leaks can occur during test runs. Therefore, the vacuum gage should be supplemented by a rugged transducer or suitable settling chamber to enable continuous monitoring of the rest-region conditions.

For wave speeds of about 1500 ft/s, pressure gage traces were not a sufficiently accurate means of assessing wave speeds for the 2-in. gaging distance utilized. If transducers are spread to a 6-in. spacing, then the probable timing accuracy can be guaranteed at least to ±3 percent of the oscilloscope sweep period.

Counter readings of wave speeds were preferable in all cases except for reflected waves, where the pulse-counting gates apparently were sensitive to spurious triggering by the very turbulent fields and resulting unstable wave forms that accompanied the reflections. For measurements of these wave speeds, the analysis of the paired transducer outputs was the most reliable method.

Recommendations for Additional Work

The following recommendations are suggested for the purpose of supplementing and amplifying the theoretical and experimental work described herein.

Additional theoretical work would be to examine the effect on qualitative and quantitative correlations of the various duct-flow theories with the following variations:

(1) Assume a constant γ and Z in the Rayleigh method.

(2) Allow for boundary-layer displacement thickness in computing expansion ratio at the duct exit plane in the Rayleigh method.

(3) Recompute the Fanno duct-flow theory for a variable γ and Z.

(4) Average the optimum combination of Rayleigh and Fanno methods to provide the initial conditions for an influence coefficients solution of the problem.

(5) Evaluate all methods indicated above as to time required and relative quality of results.

(6) Consider a broader range of porosity, duct to channel area ratio, and L/d.

Additional experimental work would include significant improvements in experimental techniques to enable the reduction of the data system's contribution to experimental uncertainty. The following suggestions are offered to indicate considerations that could prove fruitful in accomplishing this goal:

(1) Replace the plastic windows with glass optical flats.

(2) Consider an instrumented technique of focusing individual mirror systems in the framing camera.

(3) Consider the addition of rigid sectors for mounting adjustment screws to lock mirror positions and eliminate vibration of mirror mounts.

(4) Rigidize the camera support structure.

(5) Investigate methods of reducing pressure transducer heating while not degrading response and also methods of evaluating the effects. (Consider the use of thin-film ceramic and reflective coatings, etc.)

(6) Investigate ways of keeping the rest-region precision pressure gage in the system for static measurements that would isolate it from shock pressures when the tube is fired.

(7) Consider the use of perforated models to study the dynamic growth of boundary layers in shock tubes by the interaction of the auxiliary transmitted waves with the growing layer left behind by the primary wave.

(8) Conduct pressure-time-position studies to more critically evaluate wave field development.

(9) Include thin-film gage temperature instrumentation to obtain temperature-time-position data.

It is conceivable that the consideration of methods and implementation of these methods to accomplish these recommendations would enable improved correlation between theory and experiment in future work and would indicate other fruitful areas for fundamental investigation.

Goddard Space Flight Center
National Aeronautics and Space Administration
Greenbelt, Maryland December 14, 1971
160-20-51-12-51

REFERENCES

1. Davy, John: *The Collected Works of Sir Humphry Davy.* Vol. VI, Smith, Elder, and Co., London, 1840, pp. 2-64.

2. Payman, W.; and Wheeler, R. V.: "The Propagation of Flame Through Tubes of Small Diameter." *J. Chem. Soc.* **113**: 656-666, 1918.

3. Friedman, R.: "The Quenching of Laminar Oxyhydrogen Flames by Solid Surfaces." *Proc. 3rd Symp. Combust. Flame Explos. Phenom.,* Univ. of Wisconsin, 1948, pp. 11-120.

4. Edgerton, A. C.; Everett, A. J.; and Moore, N. P. W.: "Sintered Metals as Flame Traps." *Proc. 4th Symp. Combust. Flame Explos.,* 1953, pp. 689-695.

5. Frehen, F.; Hotop, W.; and Stempel, G.: "Flammensperren aus porosem Sintermetall." *Schweissen Schnieden* 7(115): 198-200, 1955.

6. Markstein, G. H.: *Non-Steady Flame Propagation.* Pergamon Press, 1964, pp. 165-175.

7. Oppenheim, A. K.; Urtiew, R. A.; and Stern, R. A.: "Peculiarity of Shock Impingement on Area Convergence." *Phys. Fluids* 2(4): 427-431, 1959.

8. Glass, I. I.; and Patterson, G. N.: "A Theoretical and Experimental Study of Shock Tube Flows." *J. Aeronaut. Sci.* 22: 73-100, 1955.

9. Bowman, J. E.; and Niblett, G. B. F.: "The Passage of a Plane Shock Wave Through a Wire Gauze." *Proc. Phys. Soc. London, Sect. B,* **68**: 1008-1016, 1955.

10. Dosanjh, D. S.: *Interaction of Grids With Traveling Shock Waves.* NACA TN 3680, 1956.

11. Barthel, H. O.: *On the Mechanism for the Interaction of a Plane Traveling Shock Wave Striking Rigid Grid-Like Structures Head On.* Doctoral dissertation, Univ. of Illinois, University Microfilms Publ. no. 20, 851, 1957.

12. Crist, R. A.: *The Use of Rock Filters to Attenuate Air Shocks.* AFSWC-TDR-63-27, Univ. of New Mexico, 1963.

13. Rudinger, G.: "A Shock Tube Technique to Determine Steady-Flow Losses of Orifices and Other Duct Elements." *J. Basic Eng.* **82**: 195-200, 1960.

14. Kochendorfer, F. D.; and Russo, M. D.: *Performance Characteristics of Aircraft Cooling Ejectors Having Short Cylindrical Shrouds.* NACA RM E51E01, 1951.

15. Bitondo, D.; and Lobb, R. K.: *The Design and Construction of a Shock Tube.* Toronto University Institute of Aerophysics Dept. Rept. no. 3, 1950, p. 48.

16. Shapiro, A. H.: *The Dynamics and Thermodynamics of Compressible Fluid Flow.* Vol. I. Ronald Press Co., 1953.

17. Shapiro, A. H.: *The Dynamics and Thermodynamics of Compressible Fluid Flow.* Vol. II. Ronald Press Co., 1954, pp. 992-1010.

18. Kennan, J. H.; and Kaye, J.: *Gas Tables.* John Wiley & Sons, Inc., 1965.

19. Hilsenrath, J.; Beckett, C. W.; Benedict, W. S.; Fano, L.; Hoge, H. J.; Masi, J. F.; Nuttall, R. L.; Toulouilian, Y. S.; and Woolley, H. W.: *Tables of Thermodynamic and Transport Properties of Air, Argon, etc.* Pergamon Press, 1960.

20. Deissler, R. G.: *Analysis of Turbulent Heat Transfer and Flow in the Entrance Regions of Smooth Passages.* NACA TN 3016, 1953.

21. Weir, A., Jr.; York, J. L.; and Morrison, R. B.; "Two- and Three-Dimensional Flow of Air Through Square-Edged Sonic Orifices." *Trans. ASME* 78: 481-488, 1956.

22. Koldozie, P. A.; and Van Winkle, M.: "Discharge Coefficients Through Perforated Plates." *J. AICE* 3(3): 305-312, 1957.

23. Baines, W. D.; and Peterson, E. G.: "An Investigation of Flow Through Screens." *Trans. ASME* 73(5), 467-480, 1951.

24. Yos, J. M.: *Transport Properties of Nitrogen, Hydrogen, Oxygen, and Air to 30,000°K.* Tech. Memo. RAD-TM-63-7 (Contract AF33(616)-7578), Research and Development Div., AVCO Corp., 1963.

25. Wick, R. S.: "The Effect of Boundary Layer on Sonic Flow Through an Abrupt Cross-Sectional Area Change." *J. Aeronaut. Sci.* 20(10): 675-682, 1953.

26. Korst, H. H.; Chow, W. L.; and Zumwalt, G. W.: *Research on Transonic and Supersonic Flow of a Real Fluid at Abrupt Increases in Cross Section.* M. E. Tech. Rept. 392-5 (Contract AF 18(606)-392), Engineering Experimental Station, Mech. Eng. Dept., Univ. of Illinois, 1959.

27. Wang, C. J.; Peterson, J. B.; and Anderson, R.: *Gas Flow Tables.* Rept. no. GM-TR-154, Technology Lab. Inc., Los Angeles, 1957.

28. Schweppe, J. L.: "Shock Tube Methods." *Methods for the Dynamic Calibration of Pressure Transducers,* NBS Monograph 67, U.S. Department of Commerce, 1963.

29. Glass, I. I.; and Hall, J. G.: "Shock Tubes." Sec. 1B of *Handbook of Supersonic Aerodynamics,* Navord Rept. 1488, vol. VI. GPO, 1959.

30. Bradley, J. M.: *Shock Waves in Chemistry and Physics.* John Wiley & Sons, Inc., 1962.

31. Mauldin, L. E.; and Compton, E. C.: *An Optical System for Recording Schlieren Images With a Continuous-Writing Ultra-High Speed Framing Camera.* NASA TND-4986, 1969.

32. Waldron, H. F.: *An Experimental Study of the Flow Properties Behind Strong Shock Waves in Nitrogen.* Doctoral dissertation, Univ. of Toronto, 1958.

33. *Instruction Manual for Type 555/21A/22A Oscilloscope.* Tektronix Inc., Beaverton, Oreg., 1964.

34. Kinman, K. A.: *Sweep Generator Circuits.* Circuit Concept Series, Tektronix Inc., Beaverton, Oreg., 1970.

35. McLain, W. H.: *Combustion Dynamics in Liquid Rocket Engines.* Monthly Rept. no. 18 (Contract NAS9-7566), Denver Res. Inst., Univ. of Denver, 1969.

NASA-Langley, 1972 —— 12

"The aeronautical and space activities of the United States shall be conducted so as to contribute . . . to the expansion of human knowledge of phenomena in the atmosphere and space. The Administration shall provide for the widest practicable and appropriate dissemination of information concerning its activities and the results thereof."

—NATIONAL AERONAUTICS AND SPACE ACT OF 1958

NASA SCIENTIFIC AND TECHNICAL PUBLICATIONS

TECHNICAL REPORTS: Scientific and technical information considered important, complete, and a lasting contribution to existing knowledge.

TECHNICAL NOTES: Information less broad in scope but nevertheless of importance as a contribution to existing knowledge.

TECHNICAL MEMORANDUMS: Information receiving limited distribution because of preliminary data, security classification, or other reasons.

CONTRACTOR REPORTS: Scientific and technical information generated under a NASA contract or grant and considered an important contribution to existing knowledge.

TECHNICAL TRANSLATIONS: Information published in a foreign language considered to merit NASA distribution in English.

SPECIAL PUBLICATIONS: Information derived from or of value to NASA activities. Publications include conference proceedings, monographs, data compilations, handbooks, sourcebooks, and special bibliographies.

TECHNOLOGY UTILIZATION PUBLICATIONS: Information on technology used by NASA that may be of particular interest in commercial and other non-aerospace applications. Publications include Tech Briefs, Technology Utilization Reports and Technology Surveys.

Details on the availability of these publications may be obtained from:

SCIENTIFIC AND TECHNICAL INFORMATION OFFICE

NATIONAL AERONAUTICS AND SPACE ADMINISTRATION

Washington, D.C. 20546